JACS
JOURNAL OF THE AMERICAN CHEMICAL SOCIETY
pubs.acs.org/JACS
Article

Mixed-Valent Diiron μ-Carbyne, μ-Hydride Complexes: Implications for Nitrogenase

Charles H. Arnett, Isabel Bogacz, Ruchira Chatterjee, Junko Yano,* Paul H. Oyala,* and Theodor Agapie*

Cite This: *J. Am. Chem. Soc.* 2020, 142, 18795−18813
Read Online
ACCESS | Metrics & More | Article Recommendations | Supporting Information

ABSTRACT: Binding of N_2 by the FeMo-cofactor of nitrogenase is believed to occur after transfer of 4 e^- and 4 H^+ equivalents to the active site. Although pulse EPR studies indicate the presence of two Fe-(μ-H)-Fe moieties, the structural and electronic features of this mixed valent intermediate remain poorly understood. Toward an improved understanding of this bioorganometallic cluster, we report herein that diiron μ-carbyne complex $(P_6ArC)Fe_2(\mu\text{-}H)$ can be oxidized and reduced, allowing for the first time spectral characterization of two EPR-active Fe(μ-C)(μ-H)Fe model complexes linked by a 2 e^- transfer which bear some resemblance to a pair of E_n and E_{n+2} states of nitrogenase. Both species populate $S = 1/2$ states at low temperatures, and the influence of valence (de)localization on the spectroscopic signature of the μ-hydride ligand was evaluated by pulse EPR studies. Compared to analogous data for the $\{Fe_2(\mu\text{-}H)\}_2$ state of FeMoco ($E_4(4H)$), the data and analysis presented herein suggest that the hydride ligands in $E_4(4H)$ bridge isovalent (most probably Fe^{III}) metal centers. Although electron transfer involves metal-localized orbitals, investigations of $[(P_6ArC)Fe_2(\mu\text{-}H)]^{+1}$ and $[(P_6ArC)Fe_2(\mu\text{-}H)]^{-1}$ by pulse EPR revealed that redox chemistry induces significant changes in Fe−C covalency (−50% upon 2 e^- reduction), a conclusion further supported by X-ray absorption spectroscopy, ^{57}Fe Mössbauer studies, and DFT calculations. Combined, our studies demonstrate that changes in covalency buffer against the accumulation of excess charge density on the metals by partially redistributing it to the bridging carbon, thereby facilitating multielectron transformations.

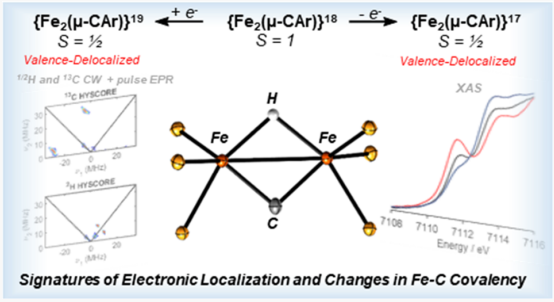

Signatures of Electronic Localization and Changes in Fe-C Covalency

INTRODUCTION

The active sites of the nitrogenase enzymes comprise a unique class of organometallic cofactors which incorporate a μ_6-C^{4-} ligand within a [7Fe-9S-M-C-*R*-homocitrate] (M = Mo, V, or Fe) cluster scaffold.[1−6] Spectroscopic and computational studies indicate that the resting state of the Mo-containing isoform (FeMoco, Figure 1, top left) is best formulated as a mixed valent Mo(III) 3Fe(II) 4Fe(III) cluster,[7−9] though the extent of valence localization is still a matter of debate.[10−13] Substrate binding and reduction require an initial electron loading phase during which the cofactor may undergo structural rearrangements.[14−17] The accumulation of reducing equivalents at FeMoco is presumably coupled to proton transfer.[18] If protonation occurs at iron (*vide infra*), this would imply that the active site may cycle through only two formal oxidation states during catalysis,[19] both of which are mixed valent. The influence of the interstitial μ_6-C^{4-} donor on the electronic structure and catalytic properties of the cofactor remains poorly understood.[20] Radiolabeling studies demonstrate that the carbide ligand is not lost or exchanged during catalysis.[21] However, this does not rule out an active role for the interstitial atom in bond breaking and bond making steps (which has been speculated previously).[22−24]

In contrast to water oxidation by photosystem II,[25] there is currently no general strategy which can generate intermediate states of FeMoco in a stepwise fashion for spectroscopic study. Sample heterogeneity complicates application of common bulk spectroscopic methods (XAS, XES or ^{57}Fe Mössbauer) to the study of reduced states of FeMoco.[13,26,27] On the other hand, CW-EPR and pulse EPR/ENDOR spectroscopies can selectively interrogate nitrogenase intermediates with half-integer spin states.[28−30] In combination with cryoannealing protocols,[31,32] these techniques have been employed to characterize a variety of putative intermediates, most notably one which has accumulated 4 e^- and 4 H^+ in the form of two Fe−(μ-H)−Fe moieties (Figure 1, top right).[33,34] It has been

Received: May 31, 2020
Published: September 25, 2020

https://dx.doi.org/10.1021/jacs.0c05920
J. Am. Chem. Soc. 2020, 142, 18795−18813

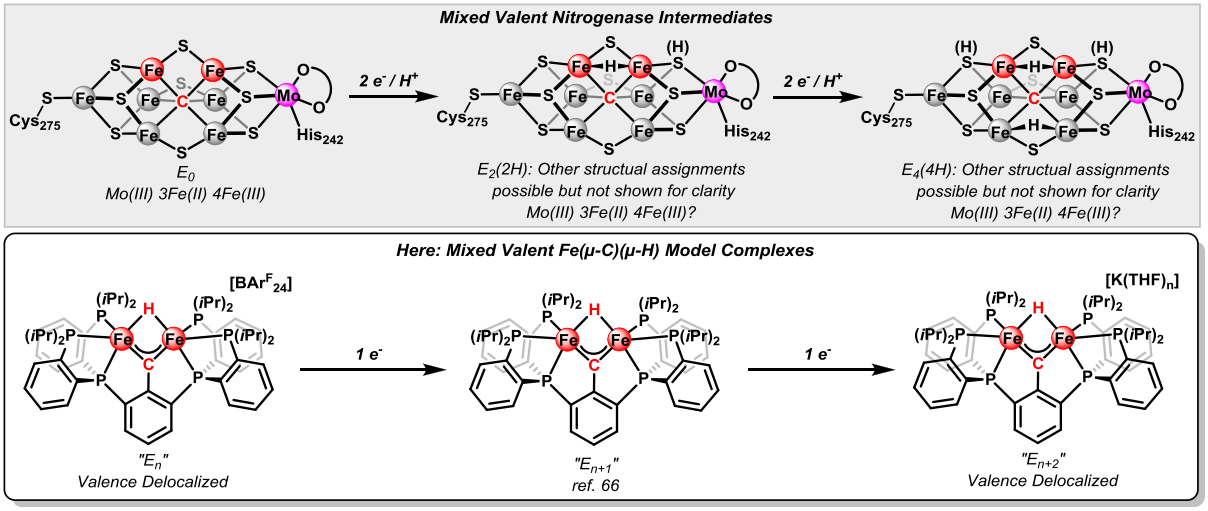

Figure 1. Mixed valent states are prevalent for the iron–molybdenum cofactor (FeMoco) of nitrogenase (top).[7−9,19] Mixed valent diiron μ-carbyne complexes are structural and electronic models of a carbon-bridged diiron subunit of FeMoco, proposed to be central to catalysis, as well as a model of the conversion of E_n to E_{n+2} (bottom).

suggested that this state is the key activated intermediate generated just prior to N_2 binding.[35,36] As such, an improved understanding of its electronic structure and geometrical features could provide crucial insight into the activation process.

Synthetic model complexes which reproduce key structural features of proposed nitrogenase intermediates can provide insight into their spectroscopic signatures. This approach has motivated EPR studies of a variety of metal complexes containing nitrogenous (Fe–N_xH_y)[37−41] and organometallic (*e.g.*, iron-alkene or iron-hydride) ligands.[42−45] Additionally, several paramagnetic diiron μ-hydride complexes have been reported,[46−53] two of which have been studied in detail using pulse EPR techniques.[54,55] These investigations elucidated the ^{1}H ENDOR signatures expected for the μ-hydride motif, at least for fully delocalized (Robin–Day Class III[56]) dimers. However, analogous studies for systems containing an Fe-(μ-C)-Fe linkage are not known, apart from a single report of pulse EPR data for the ^{13}C-labeled S = 3/2 resting state of FeMoco.[1] Carbon-bridged, multimetallic iron complexes are not uncommon,[57−65] but with few exceptions,[66−71] these species have closed shell electronic configurations. Those that are paramagnetic all exhibit integer spin states and, thus, are not readily characterized by pulse EPR methods.[66−71] To the best of our knowledge, only one synthetic iron complex featuring a carbon-based, X_n-type (n = 1,2,3) ligand with ^{13}C labeling, namely an iron(V)-carbyne complex with terminal ^{13}C-carbyne, has been interrogated by pulse EPR.[44] Enzymatic iron-alkyl species have been isotopically labeled and investigated by ENDOR and/or HYSCORE spectroscopy,[72−74] but none have been structurally characterized and questions remain regarding their electronic structure.[75,76] As such, there remains a lack of well-defined reference compounds useful for comparisons against pulse EPR data reported for FeMoco or other bioorganometallic enzymes.

Recently, we reported the synthesis and reactivity of the arylcarbyne-bridged diiron complex, (P_6ArC)Fe_2(μ-H), which features a biologically relevant Fe(μ-C)(μ-H)Fe core (Figure 1, bottom).[66] Remarkably, SQUID magnetometry revealed that (P_6ArC)Fe_2(μ-H) features a thermally well-isolated S = 1 ground state. The unusual preference of (P_6ArC)Fe_2(μ-H) to adopt an open shell configuration in spite of its strong field donor set suggested that related, mixed valence compounds might be accessible. Herein, we demonstrate that (P_6ArC)-Fe_2(μ-H) can indeed be oxidized and reduced, allowing for the first time spectral characterization of two EPR-active Fe(μ-C)(μ-H)Fe model complexes linked by a 2 e^- transfer which bear some resemblance to a pair of E_n and E_{n+2} states of nitrogenase (Figure 1, bottom).

RESULTS AND DISCUSSION

Isolation and Characterization of a Stable {Fe_2(μ-CAr)}^{17} Complex. Toward accessing EPR-active model complexes featuring a biologically relevant Fe_2(μ-C) motif, the S = 1 diiron μ-carbyne complex (P_6ArC)Fe_2(μ-H) was studied by cyclic voltammetry (CV). The CV of (P_6ArC)-Fe_2(μ-H) in tetrahydrofuran (Figure 2) exhibits two quasi-reversible electrochemical events: a reduction with $E_{1/2}$ = −2.78 V (vs Fc/Fc^+) attributed to the formation of the anionic species [(P_6ArC)Fe_2(μ-H)]$^{1-}$ and an oxidation with $E_{1/2}$ =

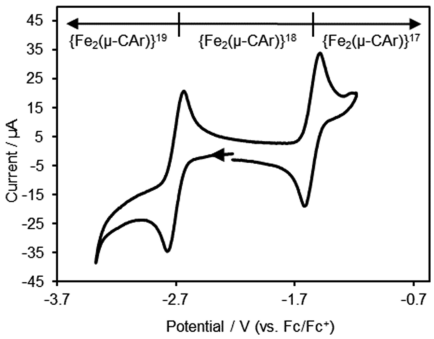

Figure 2. Cyclic voltammogram of (P_6ArC)Fe_2(μ-H) ({Fe_2(μ-CAr)}^{18}) in tetrahydrofuran (0.4 M [^{n}Bu$_4$N][PF_6] supporting electrolyte). Scan rate: 100 mV/s.

https://dx.doi.org/10.1021/jacs.0c05920
J. Am. Chem. Soc. 2020, 142, 18795−18813

−1.65 V (vs Fc/Fc^+) assigned to the generation of the corresponding cation $[(P_6ArC)Fe_2(\mu\text{-}H)]^{1+}$.[77] Although formally these electrochemical features correspond to the $Fe^{II}{}_2/Fe^{I}Fe^{II}$ and $Fe^{II}Fe^{III}/Fe^{II}{}_2$ redox couples of $(P_6ArC)Fe_2(\mu\text{-}H)$, the prospect of significant covalency within the iron−carbon bonding renders assignments of oxidation state ambiguous.[44,78−86] Fischer-type carbene and carbynes exhibit π-acidic behavior toward a low-valent metal center, though it is commonly assumed this requires heteroatom substitution at the carbene/yne C to stabilize the suboctet configuration at carbon.[87] Delocalization with the aryl substituent in **{Fe$_2$(μ-CAr)}$^{17-19}$** may impart some degree of Fischer-type character to the μ-carbyne, formally corresponding to a resonance structure of the form $\{Fe^0{}_2(\mu\text{-}CAr^+)(\mu\text{-}H^-)\}$ for **{Fe$_2$(μ-CAr)}^{18}** (Figure 3). However, in light of the high covalency of

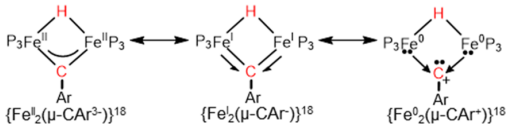

Figure 3. Limiting resonance structures for $(P_6ArC)Fe_2(\mu\text{-}H)$ (**{Fe$_2$(μ-CAr)}^{18}**).

the Fe−C bonding, a resonance form that falls between the extremes of a Fischer-type and Schrock-type description—$\{Fe^I{}_2(\mu\text{-}CAr^+)(\mu\text{-}H^-)\}$—also warrants consideration. To account for this ambiguity, the valence electron count of the $[(P_6ArC)Fe_2(\mu\text{-}H)]^{-1/0/+1}$ redox series can be described by considering both the iron 3*d* and carbyne $\sigma+\pi$ electrons (denoted *n* in $\{Fe_2(\mu\text{-}CAr)\}^n$ representation; see Figure 3 for resonance description), which is analogous to the Enemark−Feltham notation used for metal-nitrosyl complexes.[88] Thus, in this framework the formally $Fe^{II}Fe^{III}$ complex $[(P_6ArC)Fe_2(\mu\text{-}H)]^{1+}$ has a valence electron count of **{Fe$_2$(μ-CAr)}^{17}** whereas the Fe^IFe^{II} species $[(P_6ArC)Fe_2(\mu\text{-}H)]^{1-}$ is represented as **{Fe$_2$(μ-CAr)}^{19}** (Table 1).

Chemical oxidation of $(P_6ArC)Fe_2(\mu\text{-}H)$ (**{Fe$_2$(μ-CAr)}^{18}**) with $[Cp_2Co][BAr^F{}_{24}]$ in tetrahydrofuran (Figure 4a) proceeds cleanly, affording a new paramagnetic species detected by ^{1}H NMR spectroscopy (Figure S2). Single crystal X-ray diffraction (XRD) studies confirm the identity of this compound as the desired $\{Fe_2(\mu\text{-}CAr)\}^{17}$ species $[(P_6ArC)Fe_2(\mu\text{-}H)][BAr^F{}_{24}]$ (**{Fe$_2$(μ-CAr)}^{17}**, Figure 4b). Compared to **{Fe$_2$(μ-CAr)}^{18}**, oxidized **{Fe$_2$(μ-CAr)}^{17}** shows an elongation of the Fe−P bond lengths attributed to attenuated π-backbonding (Table 2). This effect is more pronounced for the equatorial P donors (Δd_{ave} = 0.066(3) Å) than for the more tightly bound P1/P4 ligands (Δd_{ave} = 0.035(3) Å). The Fe−C1 distances in **{Fe$_2$(μ-CAr)}^{17}** (Fe1−C1:1.791(6) Å, Fe2−C1:1.800(6) Å) are similar to those in **{Fe$_2$(μ-CAr)}^{18}** (Fe1/2-C1:1.792(1) Å), indicating that the redox active orbital is essentially nonbonding with respect to the carbyne ligand.

Unlike its one electron reduced congener, **{Fe$_2$(μ-CAr)}^{17}** does not have crystallographically imposed symmetry. The two iron sites of **{Fe$_2$(μ-CAr)}^{18}** are related by a C_2 axis along the C1−C2 vector (Figure 4d) which positions the metal centers on opposite faces of the central carbyne linker without any significant distortion of the C1−C2−C3−P1 torsion angle (0.36(8)°). In contrast, the solid state structure of the oxidized compound reveals that both P_3 arms have rotated such that the iron centers of **{Fe$_2$(μ-CAr)}^{17}** are oriented on the same side of the ligand (Figure 4c). This is accompanied by a deviation of the C1−C2−C3−P1 torsion angle (4.4(6)°) away from planarity.

Variable temperature ^{1}H NMR spectroscopy indicates that **{Fe$_2$(μ-CAr)}^{17}** also adopts a low symmetry structure in solution, at least below 228 K. At 298 K, the ^{1}H NMR spectrum of **{Fe$_2$(μ-CAr)}^{17}** exhibits 16 sharp, paramagnetically shifted resonances between −20 and 85 ppm (Figure S2), consistent with C_2 symmetry or an exchange process. As expected for an open shell species, cooling a solution of **{Fe$_2$(μ-CAr)}^{17}** in tetrahydrofuran-d_8 causes these features to shift substantially, with significant broadening of the signals down to 228 K (Figure 5). However, cooling below 228 K leads to decoalescence and sharpening of these features. The number of resonances (>30) observed at 188 K is roughly double that at 298 K, indicating C_1 symmetry at low temperature, in good agreement with what is observed in the solid state (T_{XRD} = 100 K). For comparison, the 1e$^-$ reduced compound **{Fe$_2$(μ-CAr)}^{18}** does not display the same behavior by variable temperature ^{1}H NMR spectroscopy[66] and, thus, either maintains a static higher symmetry geometry in solution or possesses a lower barrier to structural interconversion. Although the structure of **{Fe$_2$(μ-CAr)}^{17}** is clearly fluxional at elevated temperatures in solution, below ∼188 K the conformational changes are slow on the NMR time scale. Notably, spectroscopic studies on **{Fe$_2$(μ-CAr)}^{17}** were conducted on samples maintained at or below liquid nitrogen temperature (77 K) and, therefore, likely reflect the electronic structure of the low symmetry geometry.

Characterization of **{Fe$_2$(μ-CAr)}^{17}** by EPR spectroscopy intimates that the iron sites are antiferromagnetically coupled, leading to a doublet ground state for the dimer. The X-band ($\nu \approx 9.6$ GHz) continuous wave (CW) EPR spectrum of **{Fe$_2$(μ-CAr)}^{17}** at 5 K exhibits a nearly isotropic signal centered at $g \approx 2.09$ (Figure 6, top left), with no resolved hyperfine coupling. Measurement at Q-band ($\nu \approx 34$ GHz) via spin echo-detected field sweep resolves the small *g* anisotropy (Figure 6, bottom left), with simulations affording the rhombic *g* tensor *g* = [2.114, 2.097, 2.054]. For spin-coupled dimers in the limit of strong coupling and low zero-field splitting: $g_i = (g_1 + g_2)/2 + (g_1 - g_2)/2S(S+1)[S_1(S_1+1) - S_2(S_2+1)]$.[89,90] Thus, under the assumption of low spin Fe(II), the *g* tensor of the dimer would reflect the anisotropy of the Fe(III) site.[91] However, low spin Fe(III) complexes commonly exhibit highly anisotropic low spin signals.[92−96] Direct comparison can be made to the isoelectronic diiron μ-imide, μ-hydride complex $[([PhBP_3]Fe)_2(\mu\text{-}NH)(\mu\text{-}H)]$ which reveals the *g* anisotropy ($g_\parallel$= 2.54, $g_\perp \approx 2.04$) expected for a low spin Fe^{II}/low spin Fe^{III} spin

Table 1. Summary of Formulas for {Fe$_2$(μ-CAr)}$^{17-19}$

Full Formula	Abbreviated Core Formula (Enemark−Feltham Style)	"Classical" Oxidation State Formula
$[(P_6ArC)Fe_2(\mu\text{-}H)][BAr^F{}_{24}]$	**{Fe$_2$(μ-CAr)}^{17}**	$\{Fe^{II}(\mu\text{-}CAr)^{3-}Fe^{III}\}^{2+}$
$(P_6ArC)Fe_2(\mu\text{-}H)$	**{Fe$_2$(μ-CAr)}^{18}**	$\{Fe^{II}(\mu\text{-}CAr)^{3-}Fe^{II}\}^{+}$
$[K(THF)_n][(P_6ArC)Fe_2(\mu\text{-}H)]$	**{Fe$_2$(μ-CAr)}^{19}**	$\{Fe^{I}(\mu\text{-}CAr)^{3-}Fe^{II}\}$

https://dx.doi.org/10.1021/jacs.0c05920
J. Am. Chem. Soc. 2020, 142, 18795−18813

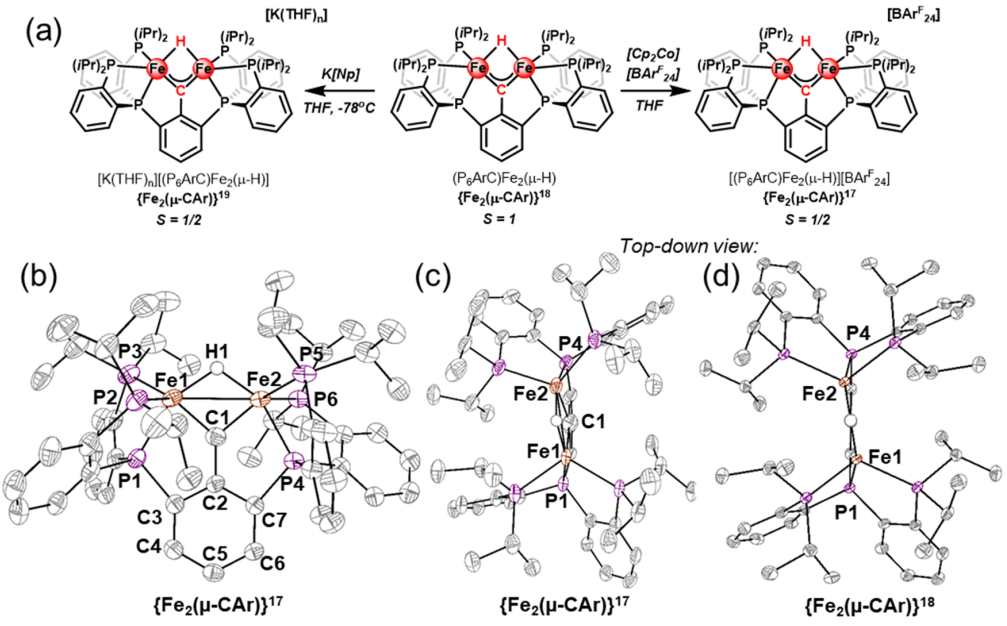

Figure 4. (a). Synthesis of $[(P_6ArC)Fe_2(\mu\text{-H})][BAr^F{}_{24}]$ ($\{\mathbf{Fe_2(\mu\text{-CAr})}\}^{17}$) and $[K(THF)_n][(P_6ArC)Fe_2(\mu\text{-H})]$ ($\{\mathbf{Fe_2(\mu\text{-CAr})}\}^{19}$) (b). Crystal structure of $[(P_6ArC)Fe_2(\mu\text{-H})][BAr^F{}_{24}]$ ($\{\mathbf{Fe_2(\mu\text{-CAr})}\}^{17}$). Hydrogen atoms on the ligand and counterion omitted for clarity. Thermal ellipsoids shown at 50% probability (c). Top down view illustrating the loss of C_2 symmetry in $[(P_6ArC)Fe_2(\mu\text{-H})][BAr^F{}_{24}]$ ($\{\mathbf{Fe_2(\mu\text{-CAr})}\}^{17}$) (d). Comparison to $P_6ArC)Fe_2(\mu\text{-H})$($\{\mathbf{Fe_2(\mu\text{-CAr})}\}^{18}$, ref 66).

Table 2. Comparison of Selected Bond Lengths and Angles for $\{\mathbf{Fe_2(\mu\text{-CAr})}\}^{17-19}$

Bonds (Å)	$\{Fe_2(\mu\text{-CAr})\}^{17}$	$\{Fe_2(\mu\text{-CAr})\}^{18a}$	$\{Fe_2(\mu\text{-CAr})\}^{19b}$
Fe1−C1	1.791(6)	1.792(1)	1.796
Fe1−P1	2.156(2)	2.1307(7)	2.076
Fe1−P2	2.292(2)	2.2627(8)	2.217
Fe1−P3	2.358(2)	2.2522(6)	2.206
Fe2−C1	1.800(6)	1.792(1)	1.796
Fe2−P4	2.176(2)	2.1307(7)	2.078
Fe2−P5	2.329(2)	2.2627(8)	2.217
Fe2−P6	2.311(2)	2.2522(6)	2.206
Fe1−Fe2	2.691(2)	2.6776(6)	2.795
Angles (deg)			
Fe1−C1−Fe2	97.0(2)	96.66(1)	102.2
Fe1−C1−C2	130.4(5)	131.67(5)	128.9
Fe2−C1−C2	130.5(5)	131.67(5)	128.9
Sum	357.9(7)	360.00(7)	360.0
P1−C3−C4	138.1(4)	141.42(1)	141.0
P4−C7−C6	138.2(4)	141.42(1)	140.8
Torsions (deg)			
C1−C2−C3−P1	4.4(6)	0.36(8)	0.2
C1−C2−C7−P4	0.4(6)	−0.36(8)	−0.3

[a]Previously reported, ref 66. [b]Structural metrics for $\{Fe_2(\mu\text{-CAr})\}^{19}$ derived from DFT geometry optimization (TPSS/def2-TZVP on Fe)).

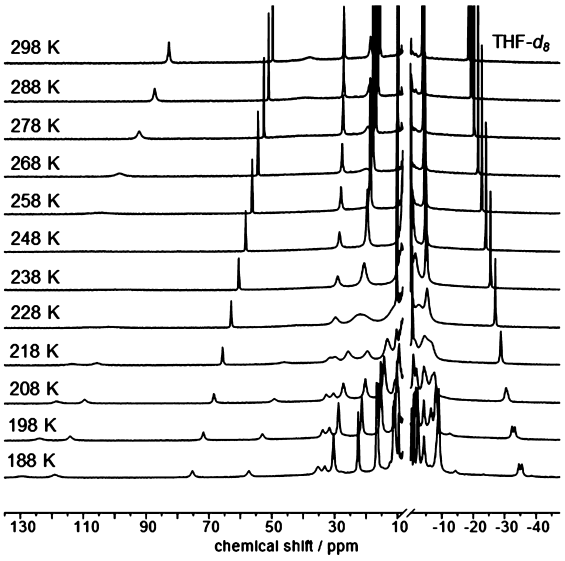

Figure 5. Variable temperature ^{1}H NMR spectra of $[(P_6ArC)Fe_2(\mu\text{-H})][BAr^F{}_{24}]$ ($\{\mathbf{Fe_2(\mu\text{-CAr})}\}^{17}$) in tetrahydrofuran-$d_8$ reveal fluxional behavior and a loss of symmetry at low temperatures.

coupled system.[55] In contrast, $\{\mathbf{Fe_2(\mu\text{-CAr})}\}^{17}$ exhibits small g anisotropy and atypical symmetry within its g tensor ($g_\perp > g_\parallel$), both of which are inconsistent with a low spin Fe(II)/low spin Fe(III) formulation.

Low-Lying Excited States in $\{Fe_2(\mu\text{-CAr})\}^{17}$. Consistent with population of higher spin states at elevated temperatures, a solution magnetic measurement of $\{\mathbf{Fe_2(\mu\text{-CAr})}\}^{17}$ provided a χT value of 1.26 cm^3 K mol^{-1} (μ_{eff} = 3.19 μ_B) at 298 K, considerably larger than that expected for an isolated S = 1/2 spin system (χT = 0.37 cm^3 K mol^{-1} and μ_{eff} = 1.73 μ_B for g = 2.00). Variable temperature magnetic susceptibility measurements on microcrystalline samples of $\{\mathbf{Fe_2(\mu\text{-CAr})}\}^{17}$ revealed a similar value for χT (1.31 cm^3 K mol^{-1}) at 298 K. The value of χT decreases as the sample is cooled down, reaching a value of 0.46 cm^3 K mol^{-1} (μ_{eff} = 1.92 μ_B) at 3 K (Figure 7).

https://dx.doi.org/10.1021/jacs.0c05920
J. Am. Chem. Soc. 2020, 142, 18795−18813

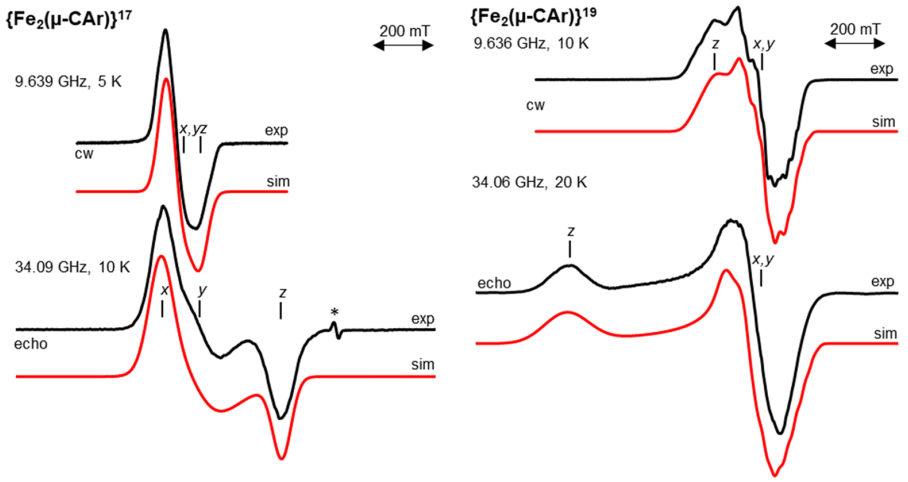

Figure 6. Left: X-band (top) and pseudomodulated[97] Q-band ESE-EPR (bottom) CW EPR spectra of $[(P_6ArC)Fe_2(\mu\text{-}H)][BAr^F{}_{24}]$ ($\{\mathbf{Fe_2(\mu\text{-}CAr)}\}^{17}$) in 2-MeTHF (2 mM). Experimental data shown in black and simulations for $S = 1/2$, $g = [2.114, 2.097, 2.054]$ are shown in red. For full simulation parameters, see the Supporting Information. The asterisk denotes a background signal present in the Q-band resonator, not in the sample. X-band Acquisition parameters: temperature = 5 K; MW frequency = 9.639 GHz; MW power = 2 mW; modulation frequency = 100 kHz; modulation amplitude = 0.4 mT; conversion time = 82 ms. Q-band Acquisition parameters: temperature = 10 K; MW frequency = 34.09 GHz. Right: X-band (top) and pseudomodulated[97] Q-band ESE-EPR (bottom) CW EPR spectra of $[K(THF)_n][(P_6ArC)Fe_2(\mu\text{-}H)]$ ($\{\mathbf{Fe_2(\mu\text{-}CAr)}\}^{19}$) in 2-MeTHF (2 mM). Experimental data shown in black, and simulations for $S = 1/2$, $g = [2.089, 2.036, 2.026]$ are shown in red. For full simulation parameters, see the Supporting Information. X-band Acquisition parameters: temperature = 10 K; MW frequency = 9.636 GHz; MW power = 2 mW; modulation frequency = 100 kHz; modulation amplitude = 0.4 mT; conversion time = 82 ms. Q-band Acquisition parameters: temperature = 20 K; MW frequency = 34.06 GHz. Note, in both cases, the X-band spectra have been shifted along the field axis for plotting purposes only.

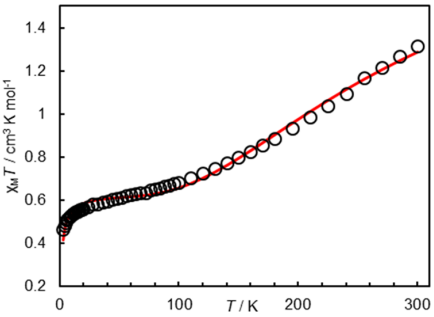

Figure 7. Variable temperature magnetic susceptibility measurements for $[(P_6ArC)Fe_2(\mu\text{-}H)][BAr^F{}_{24}]$ ($\{\mathbf{Fe_2(\mu\text{-}CAr)}\}^{17}$) collected between 3 and 300 K with a 0.5 T field after diamagnetic correction (black circles). Parameters for the fit shown: $S_1 = 1$, $g_1 = 2.55$, $S_2 = 1/2$, $g_2 = 2.45$, $J = -111.6$ cm^{-1}, $zJ = -0.64$ cm^{-1}. Equally satisfactory fits can be obtained with $S_2 = 3/2$. See Supporting Information Figure 47.

Simulations according to the Heisenberg exchange Hamiltonian $H = -2J_{12}(S_1 \cdot S_2)$ assuming $S_1 = 1$ (intermediate spin Fe(II)) and either $S_2 = 1/2$ (low spin Fe(III) or Fe(I)) or 3/2 (intermediate spin Fe(III) or high spin Fe(I)) afford isotropic exchange constants $J_{12} = -104$ cm^{-1} and -112 cm^{-1}, respectively (Figure S47). Although both models afford fits which are in reasonable agreement with the experimental data, analysis of the ^{1}H hyperfine coupling by EPR spectroscopy indicates that $\{\mathbf{Fe_2(\mu\text{-}CAr)}\}^{17}$ is valence delocalized. Efforts to simulate the magnetometry data using a more general model involving multiple spin states at arbitrary energies with $S > 1/2$ did not prove fruitful. In any case, the magnetometry data cannot be rationalized in terms of a low spin Fe(II)/low spin Fe(III) formulation, consistent with the analysis of the CW-EPR spectrum of $\{\mathbf{Fe_2(\mu\text{-}CAr)}\}^{17}$.

In Situ Characterization of a Reactive $\{\mathbf{Fe_2(\mu\text{-}CAr)}\}^{19}$ Species. To determine the effect of redox chemistry on the structural and electronic features of the Fe(μ-C)(μ-H)Fe core, we pursued characterization of the $\{\mathbf{Fe_2(\mu\text{-}CAr)}\}^{19}$ species $[K(THF)_n][(P_6ArC)Fe_2(\mu\text{-}H)]$. Treatment of $\{\mathbf{Fe_2(\mu\text{-}CAr)}\}^{18}$ with potassium naphthalenide at −78 °C generates a new species that exhibits an EPR signal centered at $g \approx 2.04$ (Figure 8a). Q-band measurements reveal that although both $\{\mathbf{Fe_2(\mu\text{-}CAr)}\}^{17}$ and $\{\mathbf{Fe_2(\mu\text{-}CAr)}\}^{19}$ exhibit axial EPR spectra, the symmetries of their g tensors are distinct (Figure 6).

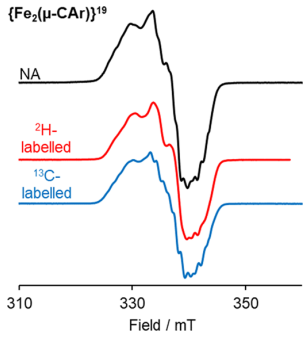

Figure 8. X-band CW EPR spectra of $[K(THF)_n][(P_6ArC)Fe_2H]$ (black), $[K(THF)_n][(P_6ArC)Fe_2D]$ (red), and $[K(THF)_n][(P_6Ar^{13}C)Fe_2H]$ (blue), all 2 mM in 2-MeTHF. Acquisition parameters: temperature = 10 K; MW frequency = 9.639 GHz; MW power = 2 mW; modulation frequency = 100 kHz; modulation amplitude = 0.4 mT; conversion time = 82 ms.

https://dx.doi.org/10.1021/jacs.0c05920
J. Am. Chem. Soc. 2020, 142, 18795−18813

Simulations indicate that $g_z > g_{x,y}$ for $\{Fe_2(\mu\text{-CAr})\}^{19}$ (g = [2.089, 2.036, 2.026]) whereas $g_{x,y} > g_z$ in $\{Fe_2(\mu\text{-CAr})\}^{17}$. Solution phase structural characterization of this species via extended X-ray absorption fine structure (EXAFS) is consistent with its assignment as $\{Fe_2(\mu\text{-CAr})\}^{19}$, with a geometry closely related to $\{Fe_2(\mu\text{-CAr})\}^{17-18}$ (Figure S55).

The signal attributed to $\{Fe_2(\mu\text{-CAr})\}^{19}$ persists and remains well-resolved for samples maintained at −78 °C for 30−60 min. Storing solutions of $\{Fe_2(\mu\text{-CAr})\}^{19}$ for >1 h. or warming above −78 °C results in loss of its characteristic EPR feature, concomitant with the appearance of several distinct S = 1/2 species (Figure S77). Thus, far, efforts to characterize these decomposition products have proved challenging. All of the iron-containing products generated at higher temperatures are NMR silent; only resonances corresponding to diisopropylphenylphosphine, derived from C−P bond cleavage of the ligand, are observed in the ^{1}H and ^{31}P NMR spectra.

^{2}H−^{1}H Pulse ENDOR/HYSCORE Supports a Symmetric Spin Distribution in $\{Fe_2(\mu\text{-CAr})\}^{17}$ and $\{Fe_2(\mu\text{-CAr})\}^{19}$. Complementary Q-band electron nuclear double resonance (ENDOR) and hyperfine sublevel correlation (HYSCORE) measurements of the ligand hyperfine coupling provide further insight into the spin distribution of $\{Fe_2(\mu\text{-CAr})\}^{17}$ and $\{Fe_2(\mu\text{-CAr})\}^{19}$. In order to determine the ^{1}H and ^{13}C hyperfine coupling, the ^{2}H and ^{13}C isotopologues were prepared (see the Supporting Information (SI) and the footnote herein).[98] Although the X-band CW-EPR spectra of the natural abundance, ^{2}H-labeled, and ^{13}C-labeled isotopologues of $\{Fe_2(\mu\text{-CAr})\}^{17}$ are broad and virtually identical (Figure S58), the isotopologues of $\{Fe_2(\mu\text{-CAr})\}^{19}$ exhibit X-band CW EPR spectra with slight differences among them (Figure 8), which are better resolved in the second derivative spectra (Figure S79). Simulation of the ^{2}H−^{1}H difference HYSCORE spectra of $[(P_6ArC)Fe_2(\mu\text{-D})][BAr^F{}_{24}]$ (Figures S59−61) affords an anisotropic deuterium hyperfine tensor $A(^2H)$ = ±[2.1, 5.5, 7.4] MHz, with a small rotation of the hyperfine tensor frame by (α,β,γ) = (15, 25, 0)° relative to the coordinate frame of the g tensor. Scaling the ^{2}H hyperfine tensor by the proportion of the ^{1}H/^{2}H gyromagnetic ratios ($^1H\gamma/^2H\gamma$ = 6.514) provides the ^{1}H hyperfine tensor $A(^1H)$ = ±[14.0, 36.0, 48.0] MHz for $\{Fe_2(\mu\text{-CAr})\}^{17}$, which is in accord with simulations of the ENDOR spectra for the natural abundance sample (Table 3).[99] In a similar manner, simulation of the HYSCORE spectra of $[K(THF)_n][(P_6ArC)Fe_2(\mu\text{-D})]$ provides, after scaling, the ^{1}H hyperfine tensor $A(^1H)$ = ±[26.0, 18.0, 41.0] MHz for $\{Fe_2(\mu\text{-CAr})\}^{19}$ (Table 3), rotated by (α,β,γ)° = (0,18,0)° relative to the frame of the g tensor. Variable mixing time ^{2}H Mims ENDOR spectra were collected on $[(P_6ArC)Fe_2(\mu\text{-D})][BAr^F{}_{24}]$ and $[K(THF)_n]$-$[(P_6ArC)Fe_2(\mu\text{-D})]$, which allowed the absolute sign of the ^{2}H hyperfine to be determined (see SI).[100] Results were consistent with the sign of the $^2H_\mu$ hyperfine (and by extension $^1H_\mu$) being negative for both $\{Fe_2(\mu\text{-CAr})\}^{17}$ and $\{Fe_2(\mu\text{-CAr})\}^{19}$.

Table 3. Hyperfine Coupling Constants in MHz Determined for $\{Fe_2(\mu\text{-CAr})\}^{17}$ and $\{Fe_2(\mu\text{-CAr})\}^{19}$[a]

$\{Fe_2(\mu\text{-CAr})\}^{17}$	A_1	A_2	A_3	a_{iso}	T
$^1H_\mu$	−14	−36	−48	−32.7	[+18.7, −3.3, −15.3]
$^{13}C_\mu$	±19	±36	±32	±29	±[+10, −7, −3]
$\{Fe_2(\mu\text{-CAr})\}^{19}$	A_1	A_2	A_3	a_{iso}	T
$^1H_\mu$	−26	−18	−41	−28.3	[+2.3, +10.3, −12.7]
$^{13}C_\mu$	±26	±30	±40	±32	±[+6, + 2, −8]

[a]All hyperfine tensors are assumed to be collinear with g except $A(^{1/2}H)$. For $\{Fe_2(\mu\text{-CAr})\}^{17}$ the Euler angles are (α,β,γ) = (15, 25, 0)°. For $\{Fe_2(\mu\text{-CAr})\}^{19}$ the Euler angles are (α,β,γ) = (0,18,0)°. The sign of $A(^{1/2}H)$ was determined by variable mixing time ^{2}H Mims ENDOR. The sign of $A(^{13}C)$ is assumed to be negative based on DFT. Seethe Supporting Information for full simulation parameters, including ^{31}P hyperfine couplings.

The ^{1}H hyperfine tensors of $\{Fe_2(\mu\text{-CAr})\}^{17}$ and $\{Fe_2(\mu\text{-CAr})\}^{19}$, respectively, can be decomposed into an isotropic component $a_{iso}(^1H)$ ($\{Fe_2(\mu\text{-CAr})\}^{17}$: −32.7 MHz, $\{Fe_2(\mu\text{-CAr})\}^{19}$:-28.3 MHz) and an anisotropic component $T(^1H)$ ($\{Fe_2(\mu\text{-CAr})\}^{17}$: [+18.7, −3.3, −15.3] MHz, $\{Fe_2(\mu\text{-CAr})\}^{19}$: [+2.3, + 10.3, −12.7] MHz). The isotropic ^{1}H hyperfine coupling arises from delocalization of spin density into the proton 1s orbital, either directly by a Fermi contact interaction or indirectly by spin polarization.[101,102] Given the large hyperfine constant expected for an electron localized in a hydrogen 1s orbital (a_{iso}^0 = 1420 MHz),[103,104] the small difference in the $a_{iso}(^1H)$ values of $\{Fe_2(\mu\text{-CAr})\}^{17}$ (−32.7 MHz) and $\{Fe_2(\mu\text{-CAr})\}^{19}$ (−28.3 MHz) implies that the spin density on the μ-hydride ligand changes by only 0.003 e^- ($\rho_s(^1H) \approx -0.023\ e^-$ and $-0.020\ e^-$, respectively) upon a 2 e^- transfer, suggesting that redox chemistry does not substantially affect the Fe−H covalency. The isotropic ^{1}H hyperfine associated with the μ-hydride ligand in $\{Fe_2(\mu\text{-CAr})\}^{17}$ can also be compared with that in the previously reported and isoelectronic μ-imide, μ-hydride species $[([PhBP_3]Fe)_2(\mu\text{-NH})(\mu\text{-H})]$.[55] Although the $a_{iso}(^1H)$ value determined for $[([PhBP_3]Fe)_2(\mu\text{-NH})(\mu\text{-H})]$ (−38.9 MHz) is larger than that in $\{Fe_2(\mu\text{-CAr})\}^{17}$ (−32.7 MHz), the differences in the μ-hydride spin densities are minimal ($\rho_s(^1H) \approx -0.027\ e^-$ and $-0.023\ e^-$, respectively).

Due to the lack of any local p-orbital contribution, the anisotropic component of the ^{1}H hyperfine arises solely from dipolar interactions with the iron-based spin. For dimeric systems, it has been shown that the full dipolar coupling tensor can be analyzed in terms of a point dipole model,[105−107] with $T(^1H)$ calculated by summing over contributions from each metal site (Figure 9).

$$T_a = -\frac{1}{2}(t_1 + t_2) \tag{1}$$

$$T_b = \frac{1}{2}(|T_a| + \frac{3}{2}*(\cos 2\gamma)^{-1}(t_1 \cos 2\beta_1 + t_2 \cos 2\beta_2)) \tag{2}$$

$$T_c = -(T_a + T_b) \tag{3}$$

$$\tan 2\gamma = (\sin 2\beta_1 - (t_2/t_1)*\sin 2\beta_2) / (\cos 2\beta_1 + (t_2/t_1)*\cos 2\beta_2) \tag{4}$$

where the values T_n (n = a, b, c) in MHz are the principal components of $T(^1H)$, β_1 and β_2 define the angle between r_1 and r_2, respectively, and the Fe1−Fe2 vector d. The angle γ describes the orientation of the coordinate axes T_b and T_c with respect to the Fe1−Fe2 vector d. The distance dependence of the magnetic dipole interaction of the μ-hydride with the individual iron centers Fe1 and Fe2, respectively, is defined by the elements t_1 and t_2 which take the classical form:

https://dx.doi.org/10.1021/jacs.0c05920
J. Am. Chem. Soc. 2020, 142, 18795−18813

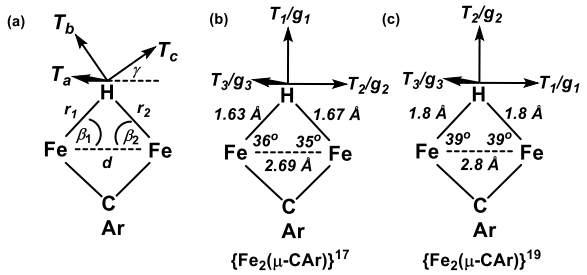

Figure 9. (a) Schematic representation of the metric parameters used to calculate the proton dipolar tensor within the defined molecular frame of $[(P_6ArC)Fe_2(\mu\text{-}H)]^n$ ($n = -1$ or $+1$).] (b) Orientation of the principal components of $T(^1H)$ in the molecular frame of $[(P_6ArC)Fe_2(\mu\text{-}H)][BAr^F{}_{24}]$ ($\{\mathbf{Fe_2(\mu\text{-}CAr)}\}^{17}$). (c) Orientation of the principal components of $T(^1H)$ in the molecular frame of $[K(THF)_n][(P_6ArC)Fe_2(\mu\text{-}H)]$ ($\{\mathbf{Fe_2(\mu\text{-}CAr)}\}^{19}$).

$$t_i = K_i c_i \left(\frac{2 g_e \beta_e g_N \beta_N}{r_i^3} \right) \tag{5}$$

where r_i represents the distance of the μ-hydride from Fe_i (i = 1,2), K_i is the spin projection coefficient for Fe_i (i = 1,2), and the effect of spin delocalization away from each Fe (such as onto the carbyne and P donor ligands) is parametrized by c_i with $0 \le c_i \le 1$.

It can be shown that a terminal hydride ligand should possess an axial anisotropic coupling tensor of the form $T(^1H) = t[-1, -1, +2]$.[43,45,108,109] On the other hand, this model predicts that a hydride which bridges two metal centers will exhibit a rhombic tensor of the form $T(^1H) = t[0, -2, +2]$.[33,54,55,110,111] For intermediate cases, the degree of rhombicity (ρ) can be quantified by decomposing the anisotropic hyperfine tensor into axial and rhombic terms, with $T = t[-(1 - \rho), -(1 + \rho), +2]$ and $\rho \to 1$ for a fully rhombic interaction. The anisotropic ^1H hyperfine coupling tensors of $\{\mathbf{Fe_2(\mu\text{-}CAr)}\}^{17}$ ($T(^1H)$ = [+18.7, −3.3, −15.3] MHz) and $\{\mathbf{Fe_2(\mu\text{-}CAr)}\}^{19}$ ($T(^1H)$ = [+2.3, + 10.3, −12.7] MHz) both exhibit a high degree of rhombicity (ρ = 0.65 and 0.64, respectively), consistent with the presence of the μ-hydride ligand. For comparison, similar deviations of the through-space dipolar coupling from $\rho \to 1$ have been reported for $[([PhBP_3]Fe)_2(\mu\text{-}NH)(\mu\text{-}H)]$ (ρ = 0.79)[55] and an $Fe^{1.5}{}_2$ bis(μ-hydride) complex (ρ = 0.75).[54]

As expressed in eq 5, the contribution of each iron center to $T(^1H)$ depends on their spin projection factors. Thus, calculations of the dipolar coupling to the μ-hydride ligand in $\{\mathbf{Fe_2(\mu\text{-}CAr)}\}^{17}$ and $\{\mathbf{Fe_2(\mu\text{-}CAr)}\}^{19}$ using the point dipole model (eqs 1−5) can shed light on the distribution of spin density and, thus, the degree of valence (de)localization in each complex. Most notably, the experimental tensor $T(^1H)_{exp}$ = [+18.7, −3.3, −15.3] MHz is distinct from those expected if $\{\mathbf{Fe_2(\mu\text{-}CAr)}\}^{17}$ was valence localized with either $S_1 = 1$, $S_2 = 1/2$ ($T(^1H)_{calc}$ = [−18, −33, +52] MHz) or $S_1 = 3/2$, $S_2 = 1/2$ ($T(^1H)_{calc}$ = [−19, −51, +70] MHz) spin coupling arrangements. On the other hand, good agreement between the experimental and calculated ($T(^1H)_{calc}$ = [+17.8, −0.2, −17.6] MHz) tensors is obtained assuming $\{\mathbf{Fe_2(\mu\text{-}CAr)}\}^{17}$ is valence delocalized ($K_1 = K_2 = +1/2$, $\gamma = 0°$) using the metric parameters r_1 = 1.63 Å, r_2 = 1.67 Å, and d = 2.69 Å (Figure 9b; see the Supporting Information for a detailed analysis). These values of r_1 and r_2 compare favorably with those determined by crystallography (Fe1−H1:1.63(3) Å, Fe2−H1:1.64(3) Å) and are similar to those reported for $[([PhBP_3]Fe)_2(\mu\text{-}NH)(\mu\text{-}H)]$ (1.64 and 1.68 Å).[55] This simulation indicates that the third principal component of $T(^1H)$ (T_3) and, thus g_3, is normal to the Fe(μ-C)(μ-H)Fe plane ($T_a = T_3$). The value of $\gamma = 0°$ indicates that the two in-plane components of $T(^1H)$ are

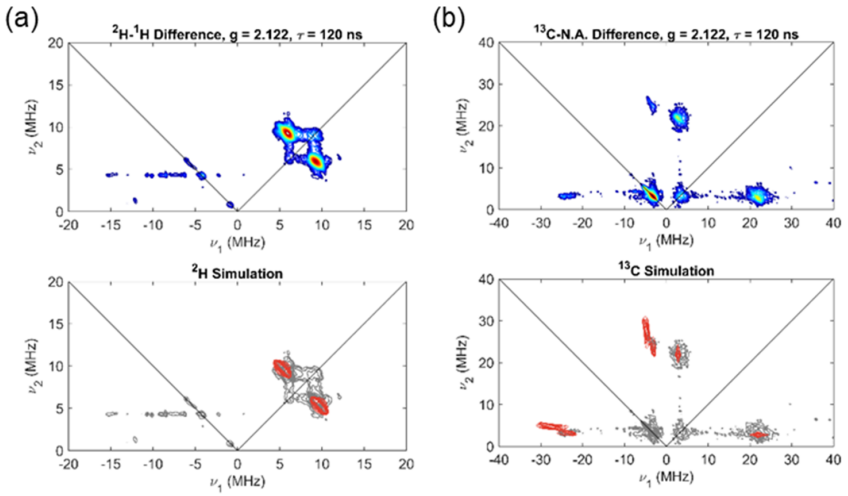

Figure 10. (a) Top panel: Q-band $^2H-^1H$ difference HYSCORE spectrum of $[(P_6ArC)Fe_2(\mu\text{-}D)][BAr^F{}_{24}]$ acquired at 1148 mT (g = 2.122). Bottom panel: Monochromatic representation of the HYSCORE data (gray) with ^2H simulations overlaid (red) using ^1H parameters in Table 3 scaled by $\gamma^2H/\gamma^1H = 0.1535$, with ^2H nuclear quadrupole parameters $e^2qQ/h = 0.15$; $\eta = 0$. Acquisition parameters: temperature = 12 K; microwave frequency = 34.086 GHz; MW pulse length ($\pi/2$, π) = 12 ns, 24 ns; τ = 120 ns, $t_1 = t_2$ = 100 ns; $\Delta t_1 = \Delta t_2$ = 12 ns; shot repetition time (srt) = 1.5 ms). (b) Top panel: Q-band ^{13}C-natural abundance difference HYSCORE spectrum of $[(P_6Ar^{13}C)Fe_2(\mu\text{-}H)][BAr^F{}_{24}]$ acquired at 1148 mT (g = 2.122). Bottom: Monochromatic representation of the HYSCORE data (gray) with ^{13}C simulations overlaid (red) using parameters in Table 3. Acquisition parameters: temperature = 12 K; microwave frequency = 34.086 GHz; MW pulse length ($\pi/2$, π) = 12 ns, 24 ns; τ = 120 ns, $t_1 = t_2$ = 100 ns; $\Delta t_1 = \Delta t_2$ = 12 ns; shot repetition time (srt) = 1.5 ms).

https://dx.doi.org/10.1021/jacs.0c05920
J. Am. Chem. Soc. 2020, 142, 18795−18813

oriented such that $T_c = T_2$ (and, therefore, g_2) lies along the Fe−Fe vector, with $T_b = T_1$ (and g_1) perpendicular to it. The orientation of $T(^1H)$ and g reported here for $\{Fe_2(\mu\text{-CAr})\}^{17}$ is distinct from that in $[([PhBP_3]Fe)_2(\mu\text{-NH})(\mu\text{-H})]$, where detailed analysis of the ^1H hyperfine coupling revealed that g_2, not g_3, is normal to the Fe(μ-N)(μ-H)Fe plane ($T_a = T_2$).[55]

Likewise, the orientation of $T(^1H)$ and g in the molecular frame of $\{Fe_2(\mu\text{-CAr})\}^{19}$ can be determined by analysis of the dipolar coupling to the μ-hydride (Figure 9). Although a solid state structure of $\{Fe_2(\mu\text{-CAr})\}^{19}$ was not obtained, the solution state structure determined by EXAFS studies is in good agreement with that predicted by DFT geometry optimizations. As such, the computationally determined metric parameters were used in the calculation of $T(^1H)$: $r_1 = r_2 = 1.79$ Å, $\beta_1 = \beta_2 = 38.7°$, $d = 2.79$ Å. DFT calculations (*vide infra*) indicate that $\{Fe_2(\mu\text{-CAr})\}^{19}$ is valence-delocalized, which implies that the spin projection factors are $K_1 = K_2 = 1/2$ and $\gamma = 0°$. The principal components of $T(^1H)$ are calculated to be $T(^1H)_{calc} = [T_c, T_b, T_a] = [+2.4, +11.4, -13.8]$ MHz, which compares favorably with the experimentally determined tensor $T(^1H) = [+2.3, +10.3, -12.7]$ MHz and validates the structural and electronic parameters assumed in the simulation. This analysis indicates that $T_a = T_3$ and, thus g_3, is normal to the Fe(μ-C)(μ-H)Fe plane (Figure 9c). The value of $\gamma = 0°$ indicates that $T_c = T_1$ (and, therefore, g_1) lies along the Fe−Fe vector. Finally, $T_b = T_2$ and g_2 are perpendicular to the Fe−Fe vector in the Fe(μ-C)(μ-H)Fe plane. Combined, analysis of the anisotropic ^1H hyperfine coupling supports an electronically delocalized description for both $\{Fe_2(\mu\text{-CAr})\}^{17}$ and $\{Fe_2(\mu\text{-CAr})\}^{19}$, implying a symmetric distribution of α and β spin density.

Pulse EPR Reveals a Decrease in Fe−C Covalency Upon Reduction. The HYSCORE spectra of the ^{13}C-labeled compounds $[(P_6Ar^{13}C)Fe_2(\mu\text{-H})][BAr^F{}_{24}]$ (Figure 10, right) and $[K(THF)_n][(P_6Ar^{13}C)Fe_2(\mu\text{-H})]$ clearly resolve the strong coupling interaction of the bridging carbon with the diiron unit (Figures S62−64). Simulations provide anisotropic hyperfine tensors $A(^{13}C) = \pm [19.0, 36.0, 32.0]$ MHz for $\{Fe_2(\mu\text{-CAr})\}^{17}$ and $A(^{13}C) = \pm [26.0, 30.0, 40.0]$ MHz for $\{Fe_2(\mu\text{-CAr})\}^{19}$, which can both be decomposed to a isotropic term $a_{iso}(^{13}C)$ ($\{Fe_2(\mu\text{-CAr})\}^{17}$: ±29.0 MHz, $\{Fe_2(\mu\text{-CAr})\}^{19}$ = ±32 MHz) and an anisotropic component $T(^{13}C)$ ($\{Fe_2(\mu\text{-CAr})\}^{17}$: $\pm[-10, +7, +3]$ MHz, $\{Fe_2(\mu\text{-CAr})\}^{19}$: $\pm[-6, -2, +8]$ MHz). The isotropic contribution to the ^{13}C coupling in $\{Fe_2(\mu\text{-CAr})\}^{19}$ ($a_{iso}(^{13}C) = \pm 32$ MHz) is greater than that in $\{Fe_2(\mu\text{-CAr})\}^{17}$ ($a_{iso}(^{13}C) = \pm 29$ MHz). However, the intrinsic coupling expected for a single electron localized in a carbon 2s orbital ($a_{iso}{}^0 = 3777$ MHz)[103,104] is much larger than these differences, signifying that the extent of Fe → C 2s spin delocalization ($\rho_s(^{13}C) \approx 7.6 \times 10^{-3}$ e^- for $\{Fe_2(\mu\text{-CAr})\}^{17}$ compared to $\sim 8.3 \times 10^{-3}$ e^- for $\{Fe_2(\mu\text{-CAr})\}^{19}$) varies only moderately with redox changes. Attempts to utilize VMT Davies ENDOR to determine the sign of the ^{13}C hyperfine coupling were unsuccessful, due to significant overlap with ENDOR transitions of ^{31}P and ^1H nuclei at both X- and Q-bands, though we note that DFT calculations indicate that the sign of $A(^{13}C)$ and $A(^{1/2}H)$ are both negative for $\{Fe_2(\mu\text{-CAr})\}^{17}$ and $\{Fe_2(\mu\text{-CAr})\}^{19}$. To the best of our knowledge, only one other synthetic iron complex featuring an anionic R_3C^-, R_2C^{2-}, or RC^{3-} type ligand has been ^{13}C enriched at the ligating carbon and interrogated by pulse EPR. This species, a terminal iron(V)-carbyne complex, was reported to have an $a_{iso}(^{13}C)$ of ±32.7 MHz,[44] which is in the range of the values observed here.

In contrast to that for the μ-hydride, the anisotropic component of the ^{13}C coupling arises from local 2p contributions, in addition to dipolar interactions with the spin localized at the adjacent Fe ions.[103] Assuming that spin polarization of the C 2p electrons is the dominant spin transfer mechanism,[112] the anisotropic ^{13}C hyperfine tensors of $\{Fe_2(\mu\text{-CAr})\}^{17}$ and $\{Fe_2(\mu\text{-CAr})\}^{19}$ can each be uniquely decomposed into two axial terms corresponding to spin transfer into the orthogonal C $2p_\sigma$ and C $2p_\pi$ orbitals (for details see SI). Deconvolution of the experimental $T(^{13}C)$ tensors affords $b_\sigma = \pm 5.7$ MHz and $b_\pi = \pm 4.3$ MHz for $\{Fe_2(\mu\text{-CAr})\}^{17}$ compared to ±1.3 MHz and ±3.3 MHz for $\{Fe_2(\mu\text{-CAr})\}^{19}$. By comparison to the orientation of the g tensor in the molecular frame, it can be shown that b_π has its largest principal component normal to the Fe(μ-C)(μ-H)Fe plane for both $\{Fe_2(\mu\text{-CAr})\}^{17}$ and $\{Fe_2(\mu\text{-CAr})\}^{19}$ (Figure 9) and is associated with spin density in the out-of-plane C $2p_\pi$ orbital. On the other hand, b_σ has its largest component in the Fe(μ-C)(μ-H)Fe plane and arises from spin density in the C 2p orbital parallel to the Fe−Fe vector. Compared to the value expected for an electron localized in a ^{13}C 2p orbital ($b^0 = 107.3$ MHz),[103,104] the values of b_σ reported here correspond to spin densities of 0.053 e^- and 0.012 e^- in the C $2p_\sigma$ orbitals of $\{Fe_2(\mu\text{-CAr})\}^{17}$ and $\{Fe_2(\mu\text{-CAr})\}^{19}$, respectively, reflecting a decrease in Fe−C σ-covalency upon reduction. Likewise, the values of b_π correspond to spin densities of 0.040 e^- and 0.031 e^- in the $2p_\pi$ orbitals of $\{Fe_2(\mu\text{-CAr})\}^{17}$ and $\{Fe_2(\mu\text{-CAr})\}^{19}$, respectively. For comparison, the degree of spin transfer into the $2p_\pi$ orbitals of the terminal carbyne ligand in $[(SiP_3)Fe^VCCH_3]^+$ is ($\rho_\pi(^{13}C) \approx \pm 0.06$ e^-).[44] Combined with $\rho(2s)$ derived from the isotropic ^{13}C coupling in $\{Fe_2(\mu\text{-CAr})\}^{19}$, the total spin density on the bridging carbon is $\sim\pm 0.051$ e^-. Notably, the total carbon spin density in $\{Fe_2(\mu\text{-CAr})\}^{17}$ ($\rho(^{13}C) \approx \pm 0.101$ e^-) is ~98% larger than that in $\{Fe_2(\mu\text{-CAr})\}^{19}$, suggesting that reduction leads to an overall decrease in Fe−C covalency.

It is also instructive to compare the 2*s* and 2*p*(π) spin densities determined by pulse EPR studies of the isoelectronic and structurally homologous complexes $\{Fe_2(\mu\text{-CAr})\}^{17}$ and $[([PhBP_3]Fe)_2(\mu\text{-NH})(\mu\text{-H})]$ to assess the relative degree of Fe−C and Fe−N covalencies. The isotropic ^{13}C hyperfine coupling in $\{Fe_2(\mu\text{-CAr})\}^{17}$ corresponds to a carbon 2s spin density ($\rho_s(^{13}C) \approx 7.6 \times 10^{-3}$ e^-) which is ~3.8 times larger than the nitrogen 2s spin density in $[([PhBP_3]Fe)_2(\mu\text{-NH})(\mu\text{-H})]$ ($\rho_s(^{14}N) \approx 2 \times 10^{-3}$ e^-).[55] Likewise, analysis of the anisotropic hyperfine coupling tensor yields a carbon 2p spin density ($\rho_p(^{13}C) \approx \pm 0.093$ e^-) for $\{Fe_2(\mu\text{-CAr})\}^{17}$ which is ~4.7 times larger than the nitrogen 2p spin density in $[([PhBP_3]Fe)_2(\mu\text{-NH})(\mu\text{-H})]$ ($\rho_p(^{14}N) \approx -0.02e^-$).[55] Overall, the data convincingly demonstrate that the Fe−C covalency in $\{Fe_2(\mu\text{-CAr})\}^{17}$ exceeds the Fe−N covalency in $[([PhBP_3]Fe)_2(\mu\text{-NH})(\mu\text{-H})]$. Consistent with the higher electronegativity of nitrogen compared to carbon, the carbyne is more easily oxidized and, therefore, develops more radical character in both its s and p orbitals.

X-ray Absorption Spectroscopy Supports Metal-Centered Redox Chemistry in $\{Fe_2(\mu\text{-CAr})\}^{17-19}$ and Reflects Redox-Induced Changes in Fe−C Covalency. The magnitude of the ^{13}C hyperfine coupling in $\{Fe_2(\mu\text{-CAr})\}^{17}$ and $\{Fe_2(\mu\text{-CAr})\}^{19}$ is inconsistent with a significant contribution of the μ-carbyne ligand to the redox-active

https://dx.doi.org/10.1021/jacs.0c05920
J. Am. Chem. Soc. 2020, 142, 18795−18813

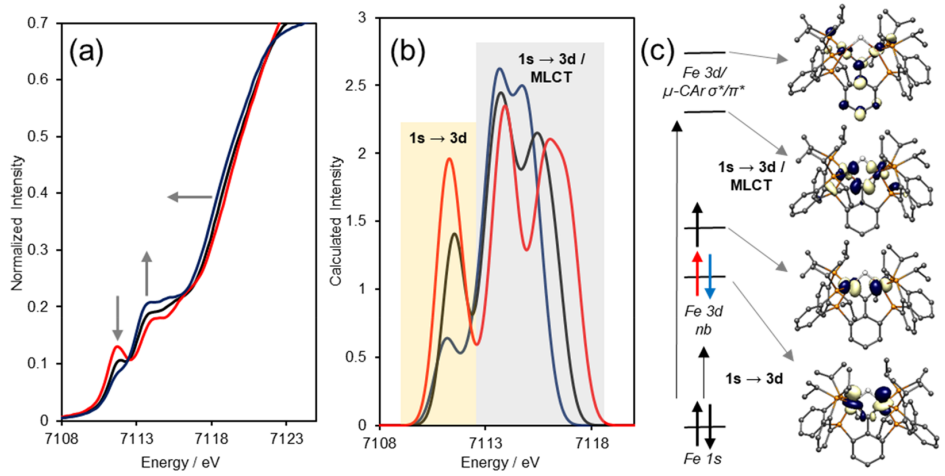

Figure 11. (a) Fe K-edge XAS spectra of $[(P_6ArC)Fe_2(\mu\text{-H})][BAr^F{}_{24}]$ ($\{\mathbf{Fe_2(\mu\text{-}CAr)}\}^{17}$, red), $(P_6ArC)Fe_2(\mu\text{-H})$ ($\{\mathbf{Fe_2(\mu\text{-}CAr)}\}^{18}$, black), and $[K(THF)_n][(P_6ArC)Fe_2(\mu\text{-H})]$ ($\{\mathbf{Fe_2(\mu\text{-}CAr)}\}^{19}$, blue) with arrows indicating the trends observed upon sequential oxidation. All samples were measured as frozen solutions (2 mM in 2-MeTHF). (b) TD-DFT calculated pre-edge XAS spectra. (c) The first pre-edge feature is assigned to transitions into two Fe 3d nonbonding orbitals, rendered on the bottom right. The higher energy features arise from acceptor states with mixed Fe 3d/μ-CAr π^* character. Quasi-restricted orbitals rendered at an isovalue of 0.05. The electrons in the nonbonding Fe 3*d* set are colored to denote the orbital population. The cation $\{\mathbf{Fe_2(\mu\text{-}CAr)}\}^{17}$ has one electron (red) in the lower energy orbital, whereas $\{\mathbf{Fe_2(\mu\text{-}CAr)}\}^{18}$ has an additional unpaired spin (black) in the higher energy orbital. Reduction to $\{\mathbf{Fe_2(\mu\text{-}CAr)}\}^{19}$ places an additional electron (blue) in the lower energy orbital.

orbital(s). To obtain a more refined picture of the changes that occur in relative iron oxidation state within the $\{\mathbf{Fe_2(\mu\text{-}CAr)}\}^{17-19}$ redox series, X-ray absorption spectra (XAS) were collected at the Fe K-edge. Consistent with redox predominantly localized at the metal sites,[113] the rising edge energies shift by 0.4−0.8 eV per oxidation event, increasing from 7118.0 eV for $\{\mathbf{Fe_2(\mu\text{-}CAr)}\}^{19}$ to 7118.4 eV for $\{\mathbf{Fe_2(\mu\text{-}CAr)}\}^{18}$ and 7119.2 eV for $\{\mathbf{Fe_2(\mu\text{-}CAr)}\}^{17}$ (Figure 11a).[114] Systematic changes are also observed in the intensity of the pre-edge, with the feature at ∼7111 eV gaining intensity upon oxidation while the features at ∼7113−7115 eV lose intensity (Figure 11a). Pre-edge transitions most commonly arise from quadrupole-allowed metal 1s → 3d transitions, which gain intensity from 3d/4p mixing in the absence of centrosymmetry.[115,116] Oxidation results in a larger number of valence holes, thereby increasing the 1s → 3d transition probability. The pre-edge intensities are also sensitive to changes in covalency with the ligand.[116] The transition probability increases with the proportion of metal character in the acceptor orbital(s) because X-ray absorption spectroscopy probes metal-localized transitions.

Time dependent DFT calculations (TPSSh/CP(PPP) on Fe) were performed to determine the origin of the pre-edge features in $\{\mathbf{Fe_2(\mu\text{-}CAr)}\}^{17-19}$.[117,118] The computations reproduce the experimentally observed trends in the relative pre-edge intensities, as well as the increased splitting of the features in the range of ∼7113−7115 eV (Figure 11b). The feature at ∼7111 eV corresponds to transitions into two low lying, iron-based orbitals of δ- and π-symmetry, respectively (Figure 11c). This pair of orbitals is predicted by DFT to be the redox-active set in $\{\mathbf{Fe_2(\mu\text{-}CAr)}\}^{17-19}$ (*vide infra*). Due to the increasing number of valence holes, the intensity of this feature increases upon oxidation.

On the other hand, the features between 7113 and 7115 eV exhibit mixed Fe 1s → 3d/carbyne character[119] and are split by transitions into two distinct acceptor orbitals (Figure 11c). The lower energy side of this region is dominated by transitions into a fairly covalent Fe−C σ^* orbital whereas the higher energy region involves transitions into the π^*-system of the μ-arylcarbyne.[120,121] The loss of intensity that occurs between 7113 and 7115 eV in the pre-edge region is consistent with an increase in iron-ligand covalency upon oxidation, identical to what was inferred based on changes in the ^{13}C hyperfine coupling in $\{\mathbf{Fe_2(\mu\text{-}CAr)}\}^{17}$ and $\{\mathbf{Fe_2(\mu\text{-}CAr)}\}^{19}$. The availability of low-lying orbitals with substantial ligand character suggests that the μ-carbyne ligand may serve a dual role as an electron donor and an electron acceptor, thereby diffusing the effects of redox chemistry at iron.

^{57}Fe Mössbauer Spectroscopy Suggests a Highly Covalent Fe−C Interaction. Similar to rising edge energies derived from Fe K-edge XAS spectra, Mössbauer isomer shifts are commonly used as an indicator of relative oxidation state.[122] Although substantial changes in isomer shift typically occur following one-electron redox changes (e.g., ∼1 mm/s for high spin, six-coordinate Fe^{II} vs ∼0.4 mm/s for high spin, six-coordinate Fe^{III}),[122] the isomer shift range observed for a structurally homologous series of compounds is highly dependent on the degree of metal−ligand covalency. Highly covalent metal−ligand interactions[78,123] provide a mechanism to prevent the accumulation of excess charge density on the metal center by distributing it onto the ligand, mitigating the effect of redox chemistry on the isomer shift.

To assess the extent of iron−carbon covalency in $\{\mathbf{Fe_2(\mu\text{-}CAr)}\}^{17-19}$, the ^{57}Fe Mössbauer spectrum of $\{\mathbf{Fe_2(\mu\text{-}CAr)}\}^{17}$ was measured as a frozen solution in 2-MeTHF with a 50 mT applied field (Figure 12, top). Although the signal can be simulated assuming only one subsite (δ = 0.23 mm s^{-1}, $|\Delta E_Q|$ = 0.70 mm s^{-1}, Figure S41), moderately improved simulations (χ^2 = 0.63 vs 1.24) were obtained by invoking two subsites. Two distinct models are obtained—one in which the two iron sites have different isomer shifts (Figure S42) and one in which they have similar isomer shifts but distinct quadrupole splittings (Figure S43). In either case, the Mössbauer signals from the individual subsites in $\{\mathbf{Fe_2(\mu\text{-}CAr)}\}^{17}$ are largely

https://dx.doi.org/10.1021/jacs.0c05920
J. Am. Chem. Soc. 2020, 142, 18795−18813

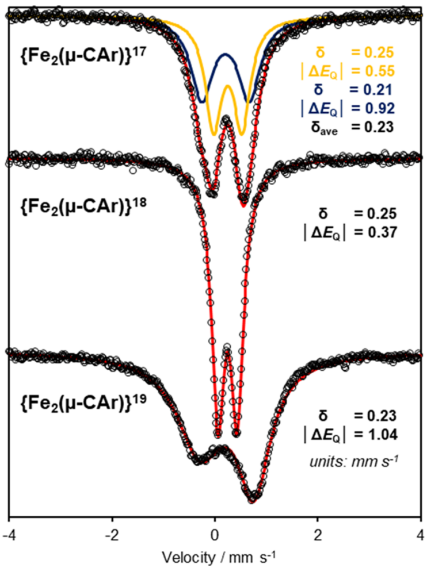

Figure 12. ^{57}Fe Mössbauer spectra of $[(P_6ArC)Fe_2(\mu\text{-H})][BAr^F{}_{24}]$ ($\{\mathbf{Fe_2(\mu\text{-}CAr)}\}^{17}$, 24 mM in 2-MeTHF, top), $(P_6ArC)Fe_2(\mu\text{-H})$ ($\{\mathbf{Fe_2(\mu\text{-}CAr)}\}^{18}$, microcrystalline solid, middle) and $[K(THF)_n][(P_6ArC)Fe_2(\mu\text{-H})]$ ($\{\mathbf{Fe_2(\mu\text{-}CAr)}\}^{19}$, 29 mM in 2-MeTHF, bottom) collected at 80 K with a 50 mT field applied parallel to γ rays. Sum fits to the experimental spectra are shown in red, with individual subsites shown in orange and blue where relevant, with parameters included. For more detailed information, see the Supporting Information.

overlapping, though a subtle shoulder may be discernible for the low velocity resonance. Overall, the model which attributes similar isomer shifts to the two iron sites comports best with the fact that $\{\mathbf{Fe_2(\mu\text{-}CAr)}\}^{17}$ is electronically delocalized, implying that the iron centers bear similar charge density.[122]

The reduced complex $\{\mathbf{Fe_2(\mu\text{-}CAr)}\}^{19}$ was also evaluated by ^{57}Fe Mössbauer spectroscopy. At 80 K, the Mössbauer spectrum of $\{\mathbf{Fe_2(\mu\text{-}CAr)}\}^{19}$ in zero applied field exhibits an asymmetric line shape and is substantially broadened (Figure S44). The spectrum is significantly sharper in the presence of a weak applied field but retains the asymmetric line shape characteristic of a system in the intermediate spin relaxation regime (Figure 12, bottom). The Mössbauer data could be simulated to one asymmetrically broadened quadrupole doublet with δ = 0.23 mm s^{-1}, $|\Delta E_Q|$ = 1.04 mm s^{-1} (Figure 12).

We previously reported that $\{\mathbf{Fe_2(\mu\text{-}CAr)}\}^{18}$ exhibits an isomer shift of 0.25 mm s^{-1} (Figure 12, middle),[66] which is nearly identical to those observed for $\{\mathbf{Fe_2(\mu\text{-}CAr)}\}^{17}$ (δ_{ave} = 0.23 mm s^{-1}) and $\{\mathbf{Fe_2(\mu\text{-}CAr)}\}^{19}$ (δ = 0.25 mm s^{-1}). The invariance of δ to one-electron redox chemistry in $\{\mathbf{Fe_2(\mu\text{-}CAr)}\}^{17-19}$, despite shifts in their rising edge energies, reflects a high degree of covalency within the Fe−C bonding. Effectively, the μ-carbyne can act as an electron source or sink, diffusing the effects of redox chemistry via through-bond interactions. As a rough gauge of how significant this influence is, a related series of mononuclear iron−carbonyl complexes $[(SiP_3)Fe(CO)]^{-1/0/+1}$ exhibit an isomer shift range that spans 0.09−0.31 mm s^{-1}.[78] More similar to that observed here, one-electron oxidation of the formally Fe(IV)-carbyne complex $[(SiP_3)FeCCH_3]$ is accompanied by a negligible change in isomer shift (−0.03 mm s^{-1} to 0.01 mm s^{-1}).[44] In both of these examples, an Fe−Si interaction provides an additional and significant pathway for covalent delocalization of charge, highlighting the relative importance of Fe−C covalency in $\{\mathbf{Fe_2(\mu\text{-}CAr)}\}^{17-19}$.

Computational Studies Support High Fe−C Covalency. A quantitative description of the Fe−C covalency in $\{\mathbf{Fe_2(\mu\text{-}CAr)}\}^{17-19}$ was also obtained from DFT calculations. Consistent with the experimental results, geometry optimizations (TPSS/ZORA-def-2-TZVP) predict that $\{\mathbf{Fe_2(\mu\text{-}CAr)}\}^{18}$ and $\{\mathbf{Fe_2(\mu\text{-}CAr)}\}^{19}$ adopt a C_2-symmetric structure in which the central carbon retains a trigonal planar conformation. Comparison of the orbital contours obtained from single-point energy calculations (TPSSh/ZORA-def2-TZVPP) on the optimized geometries of $\{\mathbf{Fe_2(\mu\text{-}CAr)}\}^{18}$ and $\{\mathbf{Fe_2(\mu\text{-}CAr)}\}^{19}$ reveals a direct correspondence in their electronic structures (Figures S102−103). Both feature molecular orbitals that are delocalized across the Fe−(μ-C)−Fe linkage, leading to a symmetric distribution of spin density on Fe1 and Fe2 (ρ(Fe) ≈ 1.11 e^- for $\{\mathbf{Fe_2(\mu\text{-}CAr)}\}^{18}$ and ρ(Fe) ≈ 0.63 e^- for $\{\mathbf{Fe_2(\mu\text{-}CAr)}\}^{19}$ based on Löwdin population analysis). The computations predict that electron transfer chemistry involves two iron-localized orbitals—one δ* symmetry orbital derived from $3d_{x^2-y^2}$ and one π* symmetry orbital of $3d_{yz}$ parentage (Figure 13). In $\{\mathbf{Fe_2(\mu\text{-}CAr)}\}^{18}$, both orbitals are singly occupied, resulting in the experimentally determined S = 1 ground state. Reduction of $\{\mathbf{Fe_2(\mu\text{-}CAr)}\}^{18}$ occurs in the nonbonding Fe−Fe δ* ($3d_{x^2-y^2}$) orbital, leaving a single unpaired α electron in the Fe−Fe π* ($3d_{yz}$).

Considering the μ-arylcarbyne in its closed shell form would infer an Fe 3d electron count of 12 for $\{\mathbf{Fe_2(\mu\text{-}CAr)}\}^{18}$ and 13 for $\{\mathbf{Fe_2(\mu\text{-}CAr)}\}^{19}$, corresponding to electronic structure descriptions of $\{Fe^{II}{}_2(\mu\text{-}CAr^{3-})(\mu\text{-}H^-)\}$and $\{Fe^{+1.5}{}_2(\mu\text{-}CAr^{3-})(\mu\text{-}H^-)\}$, respectively. However, Löwdin population analysis suggests that alternative resonance forms may be more appropriate. The $Fe_2(\mu$-C) bonding in $\{\mathbf{Fe_2(\mu\text{-}CAr)}\}^{18}$ and $\{\mathbf{Fe_2(\mu\text{-}CAr)}\}^{19}$ engages a pair of nondegenerate ligand-based σ-symmetry orbitals, which are largely localized on the bridging carbon, as well as a series of π-symmetry orbitals delocalized over the μ-arylcarbyne motif. Bonding combinations with the appropriate iron-based SALCs produces two orbitals—one corresponding to an Fe-(μ-C)-Fe σ-interaction (HOMO−8) and the other an Fe-(μ-CAr)-Fe π-bond (HOMO−7)—that are close in energy to the nonbonding Fe 3d manifold (Figure 13). Löwdin population analysis reveals that both of these orbitals exhibit substantial Fe-character (53% for HOMO−8 and 39% for HOMO−7), clearly demonstrating that the Fe−C interactions are highly covalent. As a result of this high degree of covalency, these orbitals should not be considered as predominantly ligand-based for electron counting purposes and may, in fact, be better described as part of the Fe 3d manifold. Including these electrons in the d count would result in oxidation states of $\{Fe^{I}{}_2(\mu\text{-}CAr^-)(\mu\text{-}H^-)\}$ or $\{Fe^{0}{}_2(\mu\text{-}CAr^+)(\mu\text{-}H^-)\}$ for $\{\mathbf{Fe_2(\mu\text{-}CAr)}\}^{18}$. We favor the intermediate electronic structure descriptor $\{Fe^{I}{}_2(\mu\text{-}CAr^-)(\mu\text{-}H^-)\}$, which is most representative of both the Löwdin spin population (ρ(Fe) ≈ 1.11 e^-) and the calculated atomic charges (−1.48 on Fe and −0.14 on C1). This would infer that $\{\mathbf{Fe_2(\mu\text{-}CAr)}\}^{17}$ and $\{\mathbf{Fe_2(\mu\text{-}CAr)}\}^{19}$ are best represented as $\{Fe^{+1.5}{}_2(\mu\text{-}CAr^-)(\mu\text{-}H^-)\}$ and $\{Fe^{+0.5}{}_2(\mu\text{-}CAr^-)(\mu\text{-}H^-)\}$, respectively.

DFT Calculations for $\{\mathbf{Fe_2(\mu\text{-}CAr)}\}^{17}$. Although the electronic ground state of $\{\mathbf{Fe_2(\mu\text{-}CAr)}\}^{17}$ has S = 1/2, inversion recovery experiments and magnetometry studies

https://dx.doi.org/10.1021/jacs.0c05920
J. Am. Chem. Soc. 2020, 142, 18795−18813

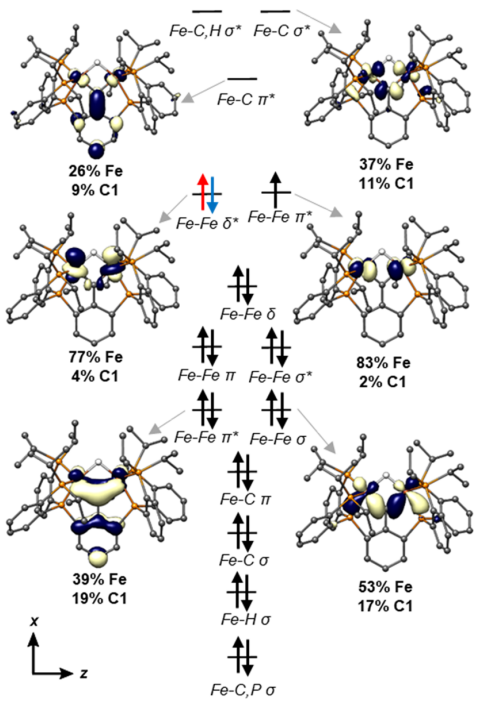

Figure 13. Qualitative molecular orbital diagram for $[(P_6ArC)Fe_2(\mu\text{-}H)][BAr^F{}_{24}]$ ($\{\mathbf{Fe_2(\mu\text{-}CAr)}\}^{17}$, red), $(P_6ArC)Fe_2(\mu\text{-}H)$ ($\{\mathbf{Fe_2(\mu\text{-}CAr)}\}^{18}$, black), and $[K(THF)_n][(P_6ArC)Fe_2(\mu\text{-}H)]$ ($\{\mathbf{Fe_2(\mu\text{-}CAr)}\}^{19}$, blue). The electrons in the nonbonding Fe 3*d* set are colored to denote the orbital population. The cation $\{\mathbf{Fe_2(\mu\text{-}CAr)}\}^{17}$ has one electron (red) in the lower energy orbital, whereas $\{\mathbf{Fe_2(\mu\text{-}CAr)}\}^{18}$ has an additional unpaired spin (black) in the higher energy orbital. Reduction to $\{\mathbf{Fe_2(\mu\text{-}CAr)}\}^{19}$ places an additional electron (blue) in the lower energy orbital. Orbital plots (isovalue = 0.05) and population analysis are shown for key Fe−C interactions and the redox-active orbitals in $\{\mathbf{Fe_2(\mu\text{-}CAr)}\}^{18}$ by way of example. Orbitals labeled by Fe−Fe interaction indicate symmetry only and do not imply the relative significance of the bonding character. Full molecular orbital diagrams are presented in the Supporting Information for each compound separately.

revealed that states with $S > 1/2$ are energetically accessible. In accord with these findings, DFT calculations on $\{\mathbf{Fe_2(\mu\text{-}CAr)}\}^{17}$ indicate that both $S = 1/2$ and $S = 3/2$ states are close in energy ($\Delta \approx 1-5$ kcal/mol, Table S9). However, only the pure DFT functional BP86 correctly predicts an $S = 1/2$ ground state for $\{\mathbf{Fe_2(\mu\text{-}CAr)}\}^{17}$—all other functionals tested provide an $S = 3/2$ ground state. In general, the calculated bond metrics for both spin states compare favorably with those determined experimentally (Table S8). Notably, the $S = 1/2$ geometry reproduces the key distortions observed in the solid state structure (Table S11), in contrast to the optimized geometry obtained for the $S = 3/2$ state of $\{\mathbf{Fe_2(\mu\text{-}CAr)}\}^{17}$, which displays C_2 symmetry. Efforts to converge to a C_2 symmetric geometry for the $S = 1/2$ state of $\{\mathbf{Fe_2(\mu\text{-}CAr)}\}^{17}$, either by starting from the optimized $S = 3/2$ geometry or from the solid state structure of $\{\mathbf{Fe_2(\mu\text{-}CAr)}\}^{18}$, were unsuccessful, consistent with the preference of $\{\mathbf{Fe_2(\mu\text{-}CAr)}\}^{17}$ to adopt lower symmetry even in solution. Although only small perturbations in the individual bond lengths and angles are observed, even subtle geometrical changes can significantly alter metal−metal communication.[124−127]

Analysis of the electronic structures derived from single-point energy calculations on the $S = 1/2$ and $3/2$ states of $\{\mathbf{Fe_2(\mu\text{-}CAr)}\}^{17}$ provide insight into the effect of structural distortion on electronic communication. As in $\mathbf{Fe_2(\mu\text{-}CAr)}\}^{18}$ and $\mathbf{Fe_2(\mu\text{-}CAr)}\}^{19}$, the $S = 3/2$ state of $\{\mathbf{Fe_2(\mu\text{-}CAr)}\}^{17}$ features molecular orbitals that are fully delocalized (Figure S101), leading to a symmetric distribution of spin density between the two iron centers (ρ(Fe) ≈ 1.65 e^- based on Löwdin population analysis). In contrast to the foregoing and at odds with ^{1}H ENDOR studies, spin-unrestricted DFT calculations on the $S = 1/2$ ground state of $\{\mathbf{Fe_2(\mu\text{-}CAr)}\}^{17}$ yield a broken-symmetry solution with substantial spin contamination (Calcd $\langle S^2\rangle$: 1.57, Theory: 0.75). Analysis of the unrestricted corresponding orbitals obtained from calculations with the TPSSh functional (10% HF) reveals a single pair of magnetic orbitals with a spatial overlap significantly less than unity ($\langle\alpha|\beta\rangle$ = 0.52, Figure S105).[128] Formally, this broken-symmetry state corresponds to antiferromagnetic coupling of an intermediate spin Fe(II) center ($S_1 = 1$) to a low spin Fe(III) ($S_2 = 1/2$). In light of the high degree of Fe−C covalency, an alternative description ($\{Fe^{I}Fe^{II}(\mu\text{-}CAr^-)(\mu\text{-}H^-)\}$) that invokes antiferromagnetic coupling to a low spin Fe(I) center ($S_2 = 1/2$) may be more appropriate.

IMPLICATIONS

Electronic (De)localization in Fe(μ-C)(μ-H)Fe Model Complexes. Calculations at the DFT level of theory suggest that the $S = 1/2$ ground state of $\{\mathbf{Fe_2(\mu\text{-}CAr)}\}^{17}$ is biased toward electronic localization whereas ^{1}H ENDOR studies clearly indicate that it is not. To understand the possible origins of this apparent discrepancy, the ratio of the delocalization energy $B(S + 1/2)$, where B is the double exchange parameter and is larger for delocalized systems, to the sum of the various trapping forces present in $\{\mathbf{Fe_2(\mu\text{-}CAr)}\}^{17}$ must be considered.[129,130] The limited solubility of $\{\mathbf{Fe_2(\mu\text{-}CAr)}\}^{18}$ as well as the thermal instability of $\{\mathbf{Fe_2(\mu\text{-}CAr)}\}^{19}$ frustrated attempts to observe intervalence charge transfer transitions in the near-IR region, which could be used to directly assess the effect of redox chemistry on the magnitude of B. However, it has been shown that the magnitude of B is proportional to the Fe−Fe σ-overlap[130] and depends strongly on the Fe−Fe distance.[126] Although a solid state structure of $\{\mathbf{Fe_2(\mu\text{-}CAr)}\}^{19}$ was not obtained, EXAFS studies suggest that the Fe−Fe separation in $\{\mathbf{Fe_2(\mu\text{-}CAr)}\}^{19}$ is longer than that in $\{\mathbf{Fe_2(\mu\text{-}CAr)}\}^{17}$, a conclusion validated by DFT geometry optimizations. Based solely on this metric, the double exchange in $\{\mathbf{Fe_2(\mu\text{-}CAr)}\}^{17}$ should be stronger, not weaker, than that in $\{\mathbf{Fe_2(\mu\text{-}CAr)}\}^{19}$. This can be verified computationally by following previously described protocols to estimate B by DFT methods,[131] which indicates a value of ∼4400 cm^{-1} for $\{\mathbf{Fe_2(\mu\text{-}CAr)}\}^{17}$ compared to only 1400 cm^{-1} for $\{\mathbf{Fe_2(\mu\text{-}CAr)}\}^{19}$, which is ∼3-fold smaller. Although ligation differences may lead to nonlinear trends in B vs r_{Fe-Fe}, the magnitude of the double exchange interactions in $\{\mathbf{Fe_2(\mu\text{-}CAr)}\}^{17}$ and $\{\mathbf{Fe_2(\mu\text{-}CAr)}\}^{19}$ predicted by DFT are likely upper bounds for the true values based on comparison with the literature ($[Fe_2(\mu\text{-}OH)_3(Me_3TACN)_2]^{2+}$: r_{Fe-Fe} = 2.51 Å, B = 1350 cm^{-1}; $[2Fe-2S]^{+}$: r_{Fe-Fe} ≈ 2.73 Å, B = 700−965 cm^{-1}).[126,130] Notwithstanding, this analysis demonstrates that, if anything, the intrinsic delocalization energy is larger for $\{\mathbf{Fe_2(\mu\text{-}CAr)}\}^{17}$ compared to $\{\mathbf{Fe_2(\mu\text{-}CAr)}\}^{19}$.

https://dx.doi.org/10.1021/jacs.0c05920
J. Am. Chem. Soc. 2020, 142, 18795−18813

However, the sum of the dynamic and static contributions to the total trapping energy may be larger in $\{\mathbf{Fe_2(\mu\text{-}CAr)}\}^{17}$ compared to $\{\mathbf{Fe_2(\mu\text{-}CAr)}\}^{19}$. Even in the absence of chemical asymmetry, electronic localization can be induced by a vibronic coupling mechanism, which involves coupling of electron and nuclear motion along a vibrational coordinate described as an antisymmetric combination of the local, metal−ligand breathing modes (*i.e.*, as the coordination sphere of one metal relaxes, the other contracts).[130] The energy associated with this term ($\Delta E_{vib} = \lambda^2/k = 4\pi^2c^2\mu\upsilon^2n(\Delta r)^2$, where μ is the reduced mass and n is the coordination number)[132] depends on the change in metal−ligand bond lengths induced by electron transfer (Δr) and the vibrational frequency (υ). If we assume, albeit crudely, that the effect per redox event on the vibrational frequency is similar to that reported for [2Fe−2S] clusters ($\upsilon_{ox}^2/\upsilon_{red}^2 \approx 1.11-1.17$),[133,134] we can estimate that the vibronic trapping energy of $\{\mathbf{Fe_2(\mu\text{-}CAr)}\}^{17}$ is ∼1.4 times ($= (\upsilon_{ox}^2/\upsilon_{red}^2)^2$) greater than that in $\{\mathbf{Fe_2(\mu\text{-}CAr)}\}^{19}$, which does not compensate for the increase in B predicted upon 2 e^- reduction.

Although geometry optimizations suggest that the iron sites of $\{\mathbf{Fe_2(\mu\text{-}CAr)}\}^{19}$ are chemically equivalent, the same is not true of $\{\mathbf{Fe_2(\mu\text{-}CAr)}\}^{17}$. Consistent with DFT calculations, ^{1}H NMR studies suggest that $\{\mathbf{Fe_2(\mu\text{-}CAr)}\}^{17}$ adopts a low symmetry solution phase structure which resembles that observed in the solid state. Comparison of the metric parameters about Fe1 and Fe2 in $\{\mathbf{Fe_2(\mu\text{-}CAr)}\}^{17}$ reveals subtle differences in the Fe−P bond lengths (Table 2). These static contributions to the total trapping energy would reinforce the vibronic trapping effect in $\{\mathbf{Fe_2(\mu\text{-}CAr)}\}^{17}$ and could promote valence localization, as predicted by DFT. However, analysis of the experimental ^{1}H hyperfine coupling clearly indicates that $\{\mathbf{Fe_2(\mu\text{-}CAr)}\}^{17}$ is valence delocalized, suggesting that DFT may not adequately describe the electronic structure of $\{\mathbf{Fe_2(\mu\text{-}CAr)}\}^{17}$. Alternatively, the ground state of $\{\mathbf{Fe_2(\mu\text{-}CAr)}\}^{17}$ *may be* localized, but at the temperature of the pulse EPR measurements (20 K), the barrier to electron hopping may be low enough that it *appears* delocalized on the EPR time scale.

Implications for Hydride-Bound Intermediates of FeMoco. A putative intermediate ($E_4(4H)$) in the reduction of N_2 by FeMoco has been freeze-trapped and characterized by EPR spectroscopy.[35] Cryoannealing experiments led Hoffman and co-workers to conclude that this species has accumulated four reducing equivalents relative to the E_0 state of FeMoco.[32] Detailed ^{1}H ENDOR studies revealed the presence of two strongly coupled protons ($a_{iso} \approx 22.3-24.3$ MHz), which were assigned to two bridging hydrides based on the rhombic symmetry of their dipolar coupling tensor ($\rho \approx 0.72-1$).[33,34] More recently, the electronic structure of this intermediate was revisited using high resolution ENDOR measurements in combination with quantum mechanical calculations.[34] This study revealed that although their hyperfine tensors are nearly coaxial, the symmetry of the dipolar coupling to each hydride is distinct, with a "null" component along g_2 for H1 (T(H1) = [−13.2, 0, +13.2] MHz) compared to a zero-value along g_3 for H2 (T(H2) = [13.2, −13.2, 0] MHz). Based on a point-dipole model for the through-space coupling of each μ-hydride to its anchor atoms, Hoffman and co-workers concluded that this permutation of the principal values of $T(^1H)$ for H1 vs H2 indicates that they bridge iron centers with distinct spin-coupling arrangements. Hoffman and co-workers suggest that H2 must bridge two metal atoms whose spins are ferromagnetically aligned (t_1, $t_2 > 0$) in order for $T(^1H)$ to have a vanishing element in the $Fe_2(\mu$-H) plane (for $T_c = -(T_a + T_b) \approx 0$, T_a must be $\sim -T_b$). On the other hand, the "null" component of T(H1) is believed to be normal to the $Fe_2(\mu$-H) plane ($T_a = -1/2(t_1 + t_2)$), which requires that $t_1 \approx -t_2$ and, thus, H1 bridges two metal centers that are antiferromagnetically coupled.

Previous ^{1}H ENDOR studies on two distinct diiron μ-hydride model complexes seem to support the foregoing conclusions. Detailed analysis of the dipolar coupling to μ-hydride in $[([PhBP_3]Fe)_2(\mu\text{-}NH)(\mu\text{-}H)]$ mapped $T(^1H)$ = [19.4, −17.4, −2.0] MHz onto the molecular frame, with g_3 in the Fe(μ-N)(μ-H)Fe plane ($T_c = T_3 \approx 0$).[55] Likewise, studies of an $[(N_2)Fe^{1.5}(\mu\text{-}H)_2Fe^{1.5}(N_2)]^-$ complex oriented the "null" component of $T(^1H)$ = [−21, 24, −3] MHz along the Fe−Fe axis.[54] Consistent with the predictions above, both complexes are formulated as fully delocalized Class III dimers and, thus, $K_1 = K_2 = +1/2$ and $t_1 = t_2 > 0$.[55,135] As discussed herein, the same is true of $\{\mathbf{Fe_2(\mu\text{-}CAr)}\}^{17}$ and $\{\mathbf{Fe_2(\mu\text{-}CAr)}\}^{19}$ and, indeed, analysis of the anisotropic ^{1}H hyperfine coupling revealed that the vanishing element corresponds to T_c in the Fe(μ-C)(μ-H)Fe plane.

Until the present study, the effect of electronic localization on the symmetry of $T(^1H)$ associated with the $Fe_2(\mu$-H) motif had not been discussed. Only one valence localized diiron μ-hydride complex is known in the literature, but pulse EPR studies have not been reported.[52] In contrast to the electronically delocalized species discussed above, a valence localized $Fe_2(\mu$-H) dimer would have an asymmetric distribution of α and β spin density. As a result, the spin projection factors K_1 and K_2 (and, thus, t_1 and t_2) would have opposite signs and unequal magnitudes. Following the analysis of Hoffman and co-workers for the dihydride state of FeMoco,[34] we would expect *a priori* that such a species would exhibit a "null" component normal to the $Fe_2(\mu$-H) plane ($T_a \approx 0$). However, as demonstrated in the Supporting Information, even if $\{\mathbf{Fe_2(\mu\text{-}CAr)}\}^{17}$ was electronically localized and antiferromagnetically coupled, T_a would *not* adopt a zero value—in fact, none of the principal components of $T(^1H)$ would be zero. Rather, the signature of valence localization in $\{\mathbf{Fe_2(\mu\text{-}CAr)}\}^{17}$ is predicted to be $|T_b| \gg |T_a|$, with $T_c \neq 0$.

To gain better physical understanding of why this is true, the effects of spin coupling must be considered carefully. Assuming local spins of $S_1 = 1$ and $S_2 = 1/2$, standard vector coupling methods[136,137] provide spin projection coefficients of $K_1 = 4/3$ and $K_2 = -1/3$, respectively, for an $S_T = 1/2$ state of $\{\mathbf{Fe_2(\mu\text{-}CAr)}\}^{17}$. If the two Fe−H bond lengths are roughly equivalent ($r_1 \approx r_2$), the magnitude of the dipolar coupling to $S_1 = 1$ is 4-fold larger than that from $S_2 = 1/2$ ($t_1 = -4t_2$, because $t_i \alpha K_i$ from eq 5). In order to achieve exact cancellation of the through-space coupling normal to the $Fe_2(\mu$-H) plane ($T_a = -1/2(t_1 + t_2) \approx 0$ when $t_1 \approx -t_2$), the distance of the μ-hydride to the iron bearing the minority spin ($S_2 = 1/2$) must be ∼1.6-fold smaller ($|K_1/K_2| = (r_1/r_2)^3 = 4$), which is not physically reasonable. A similar conclusion can be reached if instead the local spin states are $S_1 = 5/2$ (high spin Fe(III), $K_1 = +7/3$) and $S_2 = 2$ (high spin Fe(II), $K_2 = -4/3$), though the difference in the individual bond lengths necessary to achieve $T_a \approx 0$ is smaller ($|K_1/K_2| = (r_1/r_2)^3 = 7/4$; $r_1 \approx 1.2r_2$) but still substantial. It is important to note that the conclusion $T_a \neq 0$ for valence localized systems is valid for all values of γ because T_a has no angular dependence.

https://dx.doi.org/10.1021/jacs.0c05920
J. Am. Chem. Soc. 2020, 142, 18795−18813

Simultaneously, the presence of two ions with spin projection factors of unequal magnitude leads to a ^{1}H dipolar coupling tensor with $|T_b| \gg |T_a|$. Unlike the component of the anisotropic hyperfine normal to $Fe_2(\mu$-H) plane (T_a), the in-plane component T_b is very sensitive to the value of γ, which is determined from the ratio of t_2/t_1 and the angles β_1 and β_2. For a symmetrically bridged, valence delocalized $Fe_2(\mu$-H) dimer, $\gamma \equiv 0$ because $t_1 = t_2$ (see eq 4). However, when $t_1 \neq t_2$, $\gamma \neq 0$ and a factor of $(\cos 2\gamma)^{-1}$ must be included in the calculation of T_b. As illustrated in the Supporting Information, the value of γ obtained by assuming a valence localized assignment for $\{\mathbf{Fe_2(\mu\text{-}CAr)}\}^{17}$ is such that $(\cos 2\gamma)^{-1}$ contributes a factor of 5 to the calculation of T_b, leading to $|T_b| \gg |T_a|$. The relation $|T_b| \gg |T_a|$ is also true if the local spin states are $S_1 = 5/2$ (high spin Fe(III), $K_1 = +7/3$) and $S_2 = 2$ (high spin Fe(II), $K_2 = -4/3$). In fact, in this case, the value of γ is such that the factor $(\cos 2\gamma)^{-1}$ in the calculation of T_b is ∼13.

The possibility of making inferences regarding the distribution of electron density in reduced states of FeMoco is intriguing,[13] since, thus far, direct information in this regard is available only for the resting state.[8] Consistent with the study by Hoffman and co-workers,[34] we show here that the orientation and symmetry of $T(^1\text{H})$ for a bridging hydride ligand can provide valuable information about the electronic structure of the anchoring metal atoms. As concluded by them,[34] exact cancellation of the out-of-plane element T_a does in fact demonstrate that the two anchor metal atoms are antiferromagnetically coupled. Given that $T_a = 0$ for the hydride denoted H1 in the E_4(4H) state of FeMoco, it is *most likely* that H1 bridges a pair of Fe(III) metal centers ($K_1 = K_2$ so $t_1 \approx -t_2$).

However, while this T_a cancellation behavior might be true of isovalent ions, our results indicate that an *antiferromagnetically* coupled mixed valent pair will *not* exhibit this same symmetry. This is relevant to the hydride denoted H2 in the E_4(4H) state of FeMoco, wherein the vanishing element of $T(^1\text{H})$ is oriented within the $Fe_2(\mu$-H) plane ($T_c \approx 0$), which indicates that the metal centers are ferromagnetically aligned spins, either in the same oxidation state or as a delocalized pair. The symmetry of T(H2) = [13.2, −13.2, 0] MHz ($T_c = 0$) alone does not distinguish between these two valence cases for the electronic structure of the iron centers that bind H2. Rather, as emphasized by Hoffman and co-workers, it is also the fact that the principal components of T(H1) and T(H2) have identical magnitudes, though permuted, which suggests that the $Fe_2(\mu$-H1) and $Fe_2(\mu$-H2) motifs differ only in their spin coupling arrangement, not in their oxidation state. Thus, it is likely that H2 also bridges two Fe(III) ions, only these are ferromagnetically aligned, in contrast to those that bind H1.

Insight into the Electronic Structure and Reactivity of FeMoco from Pulse EPR of ^{13}C Isotopologs. Fundamental to elucidating the role of the interstitial carbide is an understanding of the nature of the Fe−C bonding and how this bonding may change during the catalytic cycle. Empirical force field simulations of nuclear resonance vibrational spectroscopic (NRVS) data for FeMoco yielded Fe−C force constants which were an order of magnitude smaller than those for low spin iron-carbide-carbonyl clusters.[138] Reduction and/or substrate binding to FeMoco may induce further weakening and elongation of the Fe−C bond(s).[139−141] This has been demonstrated for some monometallic iron-alkyl model complexes and has been attributed to the ionic character of the bond, which becomes more polarized upon reduction.[142,143] Notably, enhanced N_2 reduction reactivity was observed for systems featuring more flexible axial donors.[142] However, more recent QM/MM studies accounting for the effects of antiferromagnetic coupling within the cluster afforded Fe−C force constants roughly five times larger than suggested from computational modeling of NRVS data.[144] Further support of more highly covalent bonding to the interstitial carbide was obtained by XES studies, which revealed a decrease in the splitting of the Fe Kβ mainlines of FeMoco and FeVco compared to that in $MoFe_3S_4$ and VFe_3S_4 cubane models.[145]

The lack of a consistent description of the Fe−C bonding in FeMoco motivates complementary studies aimed at benchmarking Fe−C covalency. In principle, ligand hyperfine couplings can provide a direct and comparable measure of metal−ligand interactions.[101,146−148] However, theoretical studies of FeMoco revealed a significant dependence of $a_{iso}(\mu_6$-X) (assumed at that time to be N^{3-}, but equally valid for C^{4-}) on the specific spin coupling arrangement of the cofactor.[149] The lowest energy BS7 solution has a symmetric distribution of "spin-up" and "spin-down" density around the central atom, which results in a small isotropic coupling. As a result, the relative degree of Fe−C covalency in FeMoco cannot be assessed based on a comparison with the a_{iso} or $\rho(^{13}\text{C})$ values reported here.

The present pulse EPR and XAS studies support the hypothesis that electron loading leads to a decrease in Fe−C covalency, at least in a $Fe_2(\mu$-C) model system. Although the carbon 2s and 2p spin densities of $\{\mathbf{Fe_2(\mu\text{-}CAr)}\}^{17}$ ($\rho(^{13}\text{C}) \approx \pm 0.101\ e^-$) and $\{\mathbf{Fe_2(\mu\text{-}CAr)}\}^{19}$ ($\rho(^{13}\text{C}) \approx \pm 0.051\ e^-$) are similar in absolute terms, in terms of percent change, 2 e^- reduction leads to a significant decrease (∼50%) in Fe−C covalency. This trend is in reasonable agreement with the predicted change in the calculated covalency[150] of C1, which decreases from 31.7% in $\{\mathbf{Fe_2(\mu\text{-}CAr)}\}^{17}$ to 15.6% in $\{\mathbf{Fe_2(\mu\text{-}CAr)}\}^{19}$ based on DFT. Deconvolution of the anisotropic component of the ^{13}C hyperfine coupling in $\{\mathbf{Fe_2(\mu\text{-}CAr)}\}^{17}$ and $\{\mathbf{Fe_2(\mu\text{-}CAr)}\}^{19}$ revealed that redox chemistry disparately affects the Fe−C σ- and π-bonding, with a significant decrease in σ-covalency and a less substantial change in π-covalency upon reduction. Notably, these changes in Fe−C covalency occur despite the fact that redox chemistry involves metal-localized orbitals. A similar observation has been made for some [Fe−S] clusters (13−16% decrease in Fe−S covalency upon $1e^-$ reduction) and has been attributed to electronic relaxation that accompanies the redox process.[150] Even in the absence of significant structural differences, changes in the electron−electron repulsion induced by metal-based redox chemistry can trigger a redistribution of the charge density to the ligands via changes in covalency. This model of electronic relaxation via changes in Fe−C covalency is clearly in accord with our ^{57}Fe Mossbauer studies, which revealed that $\{\mathbf{Fe_2(\mu\text{-}CAr)}\}^{17-19}$ have nearly identical (average) isomer shifts. The interstitial carbide of FeMoco may also serve as a source or sink of electron density by modulating the degree of Fe−C covalency, helping to prevent the accumulation of excess charge density at iron and facilitating multielectron transformations.

CONCLUSION

The diiron μ-carbyne complexes $\{\mathbf{Fe_2(\mu\text{-}CAr)}\}^{17}$ and $\{\mathbf{Fe_2(\mu\text{-}CAr)}\}^{19}$ are the first carbon-bridged, dinuclear iron complexes that feature odd numbers of valence electrons. Both species

https://dx.doi.org/10.1021/jacs.0c05920
J. Am. Chem. Soc. 2020, 142, 18795−18813

populate $S = 1/2$ states at low temperature and spectroscopic studies reveal that both are valence delocalized. Both $\{Fe_2(\mu\text{-}CAr)\}^{17}$ and $\{Fe_2(\mu\text{-}CAr)\}^{19}$ were amenable to investigation by pulse EPR methods, affording a unique opportunity to assess the influence of valence (de)localization on the spectroscopic signature of the μ-hydride ligand. Caution must be exercised when interpreting the orientation and symmetry of $T(^1H)$ for a bridging hydride in terms of the spin-coupling of the anchoring metal atoms. However, combined with a study by Hoffman and co-workers,[34] our results suggest that the hydride ligands in the $\{Fe_2(\mu\text{-}H)\}_2$ intermediate $E_4(4H)$ bridge isovalent (most probably Fe^{III}) metal centers, providing valuable insight into the distribution of electron density in a reduced state of FeMoco.

Although DFT calculations indicate that electron transfer involves metal-localized orbitals, pulse EPR investigations of $\{Fe_2(\mu\text{-}^{13}CAr)\}^{17}$ and $\{Fe_2(\mu\text{-}^{13}CAr)\}^{19}$ revealed that redox chemistry induces significant changes in Fe−C covalency (−50% upon 2 e^- reduction), a conclusion further supported by X-ray absorption spectroscopy, ^{57}Fe Mössbauer studies, and computational studies. Although the relative degree of Fe−C covalency in FeMoco cannot be directly assessed based on a comparison with the a_{iso} or $\rho(^{13}C)$ values reported here, computational studies suggest that ^{13}C hyperfine interaction may still be a valuable reporter of structural and/or electronic deformations that reduce the symmetry of the cofactor.[139] Although use of ^{13}C-S-adenosylmethionine allows the biosynthesis of FeMoco with the interstitial carbide selectively labeled with ^{13}C, there is currently only one report of ^{13}C ESEEM targeting the central atom, specifically for the $S = 3/2$ resting state of FeMoco.[1] Further studies of the ^{13}C-labeled cofactor are expected to be informative since pulse EPR methods have proven insightful for understanding the structural and electronic features of the cofactor in a variety of states.[28−30] These efforts, in concert with theoretical and synthetic modeling of the structural and spectroscopic features of FeMoco, may help to better elucidate the nature of the activation process.

■ ASSOCIATED CONTENT

Supporting Information

The Supporting Information is available free of charge at https://pubs.acs.org/doi/10.1021/jacs.0c05920.

Crystallographic data for $\{Fe_2(\mu\text{-}CAr)\}^{17}$ (CIF)

Synthetic procedures, characterization data, spectroscopic data, and computational results (PDF)

■ AUTHOR INFORMATION

Corresponding Authors

Theodor Agapie − *Division of Chemistry and Chemical Engineering, California Institute of Technology, Pasadena, California 91125, United States;* orcid.org/0000-0002-9692-7614; Email: agapie@caltech.edu

Paul H. Oyala − *Division of Chemistry and Chemical Engineering, California Institute of Technology, Pasadena, California 91125, United States;* orcid.org/0000-0002-8761-4667; Email: phoyala@caltech.edu

Junko Yano − *Molecular Biophysics and Integrated Bioimaging Division, Lawrence Berkeley National Laboratory, Berkeley, California 94720, United States;* orcid.org/0000-0001-6308-9071; Email: jyano@lbl.gov

Authors

Charles H. Arnett − *Division of Chemistry and Chemical Engineering, California Institute of Technology, Pasadena, California 91125, United States;* orcid.org/0000-0002-1272-3797

Isabel Bogacz − *Molecular Biophysics and Integrated Bioimaging Division, Lawrence Berkeley National Laboratory, Berkeley, California 94720, United States;* orcid.org/0000-0003-1493-3867

Ruchira Chatterjee − *Molecular Biophysics and Integrated Bioimaging Division, Lawrence Berkeley National Laboratory, Berkeley, California 94720, United States;* orcid.org/0000-0002-0865-061X

Complete contact information is available at: https://pubs.acs.org/10.1021/jacs.0c05920

Notes

The authors declare no competing financial interest.

■ ACKNOWLEDGMENTS

We are grateful to the NSF for funding (CHE-1905320 to T.A. and an NSF Graduate Research Fellowship to C.H.A.). We thank Prof. Jonas C. Peters and Prof. Ryan G. Hadt for insightful discussions and Prof. Peters for the use of his group's Mössbauer spectrometer. We thank Michael Takase and Lawrence Henling for assistance with X-ray crystallography and David VanderVelde for assistance with NMR spectroscopy. Magnetic data was acquired at the University of California, Los Angeles with assistance from Dr. Ignacio Martini on a Quantum Design MPMS3 SQUID Magnetometer supported by the NSF (MRI-1625776). Support has been provided for the Caltech EPR Facility via an NSF grant (1531940) and the Dow Next Generation Educator Fund, which is also acknowledged for support of the X-ray diffraction and NMR instrumentation. The computations presented here were conducted on the Caltech High Performance Cluster partially supported by a grant from the Gordon and Betty Moore Foundation.

■ REFERENCES

(1) Spatzal, T.; Aksoyoglu, M.; Zhang, L.; Andrade, S. L. A.; Schleicher, E.; Weber, S.; Rees, D. C.; Einsle, O. Evidence for Interstitial Carbon in Nitrogenase FeMo Cofactor. *Science* **2011**, *334* (6058), 940−940.

(2) Einsle, O.; Tezcan, F. A.; Andrade, S. L. A.; Schmid, B.; Yoshida, M.; Howard, J. B.; Rees, D. C. Nitrogenase MoFe-Protein at 1.16 Å Resolution: A Central Ligand in the FeMo-Cofactor. *Science* **2002**, *297* (5587), 1696−1700.

(3) Kirn, J.; Rees, D. C. Crystallographic structure and functional implications of the nitrogenase molybdenum−iron protein from Azotobacter vinelandii. *Nature* **1992**, *360*, 553.

(4) Lancaster, K. M.; Roemelt, M.; Ettenhuber, P.; Hu, Y.; Ribbe, M. W.; Neese, F.; Bergmann, U.; DeBeer, S. X-ray Emission Spectroscopy Evidences a Central Carbon in the Nitrogenase Iron-Molybdenum Cofactor. *Science* **2011**, *334* (6058), 974−977.

(5) Rees, J. A.; Bjornsson, R.; Schlesier, J.; Sippel, D.; Einsle, O.; DeBeer, S. The Fe−V Cofactor of Vanadium Nitrogenase Contains an Interstitial Carbon Atom. *Angew. Chem., Int. Ed.* **2015**, *54* (45), 13249−13252.

(6) Sippel, D.; Einsle, O. The structure of vanadium nitrogenase reveals an unusual bridging ligand. *Nat. Chem. Biol.* **2017**, *13*, 956.

(7) Bjornsson, R.; Lima, F. A.; Spatzal, T.; Weyhermuller, T.; Glatzel, P.; Bill, E.; Einsle, O.; Neese, F.; DeBeer, S. Identification of a spin-coupled Mo(III) in the nitrogenase iron-molybdenum cofactor. *Chem. Sci.* **2014**, *5* (8), 3096−3103.

(8) Spatzal, T.; Schlesier, J.; Burger, E.-M.; Sippel, D.; Zhang, L.; Andrade, S. L. A.; Rees, D. C.; Einsle, O. Nitrogenase FeMoco investigated by spatially resolved anomalous dispersion refinement. *Nat. Commun.* **2016**, *7*, 10902.
(9) Kowalska, J. K.; Henthorn, J. T.; Van Stappen, C.; Trncik, C.; Einsle, O.; Keavney, D.; DeBeer, S. X-ray Magnetic Circular Dichroism Spectroscopy Applied to Nitrogenase and Related Models: Experimental Evidence for a Spin-Coupled Molybdenum(III) Center. *Angew. Chem., Int. Ed.* **2019**, *58* (28), 9373−9377.
(10) Bjornsson, R.; Neese, F.; DeBeer, S. Revisiting the Mössbauer Isomer Shifts of the FeMoco Cluster of Nitrogenase and the Cofactor Charge. *Inorg. Chem.* **2017**, *56* (3), 1470−1477.
(11) Benediktsson, B.; Bjornsson, R. QM/MM Study of the Nitrogenase MoFe Protein Resting State: Broken-Symmetry States, Protonation States, and QM Region Convergence in the FeMoco Active Site. *Inorg. Chem.* **2017**, *56* (21), 13417−13429.
(12) Kowalska, J. K.; Hahn, A. W.; Albers, A.; Schiewer, C. E.; Bjornsson, R.; Lima, F. A.; Meyer, F.; DeBeer, S. X-ray Absorption and Emission Spectroscopic Studies of [L2Fe2S2]n Model Complexes: Implications for the Experimental Evaluation of Redox States in Iron−Sulfur Clusters. *Inorg. Chem.* **2016**, *55* (9), 4485−4497.
(13) Henthorn, J. T.; Arias, R. J.; Koroidov, S.; Kroll, T.; Sokaras, D.; Bergmann, U.; Rees, D. C.; DeBeer, S. Localized Electronic Structure of Nitrogenase FeMoco Revealed by Selenium K-Edge High Resolution X-ray Absorption Spectroscopy. *J. Am. Chem. Soc.* **2019**, *141* (34), 13676−13688.
(14) Buscagan, T. M.; Rees, D. C. Rethinking the Nitrogenase Mechanism: Activating the Active Site. *Joule* **2019**, *3* (11), 2662−2678.
(15) Spatzal, T.; Perez, K. A.; Howard, J. B.; Rees, D. C. Catalysis-dependent selenium incorporation and migration in the nitrogenase active site iron-molybdenum cofactor. *eLife* **2015**, *4*, No. e11620.
(16) Spatzal, T.; Perez, K. A.; Einsle, O.; Howard, J. B.; Rees, D. C. Ligand binding to the FeMo-cofactor: Structures of CO-bound and reactivated nitrogenase. *Science* **2014**, *345* (6204), 1620−1623.
(17) Sippel, D.; Rohde, M.; Netzer, J.; Trncik, C.; Gies, J.; Grunau, K.; Djurdjevic, I.; Decamps, L.; Andrade, S. L. A.; Einsle, O. A bound reaction intermediate sheds light on the mechanism of nitrogenase. *Science* **2018**, *359* (6383), 1484−1489.
(18) Morrison, C. N.; Spatzal, T.; Rees, D. C. Reversible Protonated Resting State of the Nitrogenase Active Site. *J. Am. Chem. Soc.* **2017**, *139* (31), 10856−10862.
(19) Doan, P. E.; Telser, J.; Barney, B. M.; Igarashi, R. Y.; Dean, D. R.; Seefeldt, L. C.; Hoffman, B. M. ^{57}Fe ENDOR Spectroscopy and 'Electron Inventory' Analysis of the Nitrogenase E_4 Intermediate Suggest the Metal-Ion Core of FeMo-Cofactor Cycles Through Only One Redox Couple. *J. Am. Chem. Soc.* **2011**, *133* (43), 17329−17340.
(20) Čorić, I.; Holland, P. L. Insight into the Iron−Molybdenum Cofactor of Nitrogenase from Synthetic Iron Complexes with Sulfur, Carbon, and Hydride Ligands. *J. Am. Chem. Soc.* **2016**, *138* (23), 7200−7211.
(21) Wiig, J. A.; Lee, C. C.; Hu, Y.; Ribbe, M. W. Tracing the Interstitial Carbide of the Nitrogenase Cofactor during Substrate Turnover. *J. Am. Chem. Soc.* **2013**, *135* (13), 4982−4983.
(22) Siegbahn, P. E. M. The mechanism for nitrogenase including all steps. *Phys. Chem. Chem. Phys.* **2019**, *21* (28), 15747−15759.
(23) Siegbahn, P. E. M. Model Calculations Suggest that the Central Carbon in the FeMo-Cofactor of Nitrogenase Becomes Protonated in the Process of Nitrogen Fixation. *J. Am. Chem. Soc.* **2016**, *138* (33), 10485−10495.
(24) McKee, M. L. A New Nitrogenase Mechanism Using a CFe_8S_9 Model: Does H2 Elimination Activate the Complex to N_2 Addition to the Central Carbon Atom? *J. Phys. Chem. A* **2016**, *120* (5), 754−764.
(25) Yano, J.; Yachandra, V. Mn_4Ca Cluster in Photosynthesis: Where and How Water is Oxidized to Dioxygen. *Chem. Rev.* **2014**, *114* (8), 4175−4205.
(26) Van Stappen, C.; Thorhallsson, A. T.; Decamps, L.; Bjornsson, R.; DeBeer, S. Resolving the structure of the E_1 state of Mo nitrogenase through Mo and Fe K-edge EXAFS and QM/MM calculations. *Chem. Sci.* **2019**, *10* (42), 9807−9821.
(27) Van Stappen, C.; Davydov, R.; Yang, Z.-Y.; Fan, R.; Guo, Y.; Bill, E.; Seefeldt, L. C.; Hoffman, B. M.; DeBeer, S. Spectroscopic Description of the E_1 State of Mo Nitrogenase Based on Mo and Fe X-ray Absorption and Mössbauer Studies. *Inorg. Chem.* **2019**, *58* (18), 12365−12376.
(28) Hoffman, B. M.; Lukoyanov, D.; Yang, Z.-Y.; Dean, D. R.; Seefeldt, L. C. Mechanism of Nitrogen Fixation by Nitrogenase: The Next Stage. *Chem. Rev.* **2014**, *114* (8), 4041−4062.
(29) Hoffman, B. M.; Lukoyanov, D.; Dean, D. R.; Seefeldt, L. C. Nitrogenase: A Draft Mechanism. *Acc. Chem. Res.* **2013**, *46* (2), 587−595.
(30) Dos Santos, P. C.; Igarashi, R. Y.; Lee, H.-I.; Hoffman, B. M.; Seefeldt, L. C.; Dean, D. R. Substrate Interactions with the Nitrogenase Active Site. *Acc. Chem. Res.* **2005**, *38* (3), 208−214.
(31) Lukoyanov, D.; Yang, Z.-Y.; Duval, S.; Danyal, K.; Dean, D. R.; Seefeldt, L. C.; Hoffman, B. M. A Confirmation of the Quench-Cryoannealing Relaxation Protocol for Identifying Reduction States of Freeze-Trapped Nitrogenase Intermediates. *Inorg. Chem.* **2014**, *53* (7), 3688−3693.
(32) Lukoyanov, D.; Barney, B. M.; Dean, D. R.; Seefeldt, L. C.; Hoffman, B. M. Connecting nitrogenase intermediates with the kinetic scheme for N_2 reduction by a relaxation protocol and identification of the N_2 binding state. *Proc. Natl. Acad. Sci. U. S. A.* **2007**, *104* (5), 1451−1455.
(33) Igarashi, R. Y.; Laryukhin, M.; Dos Santos, P. C.; Lee, H.-I.; Dean, D. R.; Seefeldt, L. C.; Hoffman, B. M. Trapping H- Bound to the Nitrogenase FeMo-Cofactor Active Site during H_2 Evolution: Characterization by ENDOR Spectroscopy. *J. Am. Chem. Soc.* **2005**, *127* (17), 6231−6241.
(34) Hoeke, V.; Tociu, L.; Case, D. A.; Seefeldt, L. C.; Raugei, S.; Hoffman, B. M. High-Resolution ENDOR Spectroscopy Combined with Quantum Chemical Calculations Reveals the Structure of Nitrogenase Janus Intermediate E_4(4H). *J. Am. Chem. Soc.* **2019**, *141* (30), 11984−11996.
(35) Lukoyanov, D.; Khadka, N.; Yang, Z.-Y.; Dean, D. R.; Seefeldt, L. C.; Hoffman, B. M. Reductive Elimination of H2 Activates Nitrogenase to Reduce the N≡N Triple Bond: Characterization of the E_4(4H) Janus Intermediate in Wild-Type Enzyme. *J. Am. Chem. Soc.* **2016**, *138* (33), 10674−10683.
(36) Rohde, M.; Sippel, D.; Trncik, C.; Andrade, S. L. A.; Einsle, O. The Critical E_4 State of Nitrogenase Catalysis. *Biochemistry* **2018**, *57* (38), 5497−5504.
(37) Lees, N. S.; McNaughton, R. L.; Gregory, W. V.; Holland, P. L.; Hoffman, B. M. ENDOR Characterization of a Synthetic Diiron Hydrazido Complex as a Model for Nitrogenase Intermediates. *J. Am. Chem. Soc.* **2008**, *130* (2), 546−555.
(38) Thompson, N. B.; Oyala, P. H.; Dong, H. T.; Chalkley, M. J.; Zhao, J.; Alp, E. E.; Hu, M.; Lehnert, N.; Peters, J. C. Electronic Structures of an $[Fe(NNR_2)]$++/0/− Redox Series: Ligand Non-innocence and Implications for Catalytic Nitrogen Fixation. *Inorg. Chem.* **2019**, *58* (5), 3535−3549.
(39) Nesbit, M. A.; Oyala, P. H.; Peters, J. C. Characterization of the Earliest Intermediate of Fe-N_2 Protonation: CW and Pulse EPR Detection of an Fe-NNH Species and Its Evolution to Fe-NNH_2^{+2}. *J. Am. Chem. Soc.* **2019**, *141* (20), 8116−8127.
(40) Anderson, J. S.; Cutsail, G. E.; Rittle, J.; Connor, B. A.; Gunderson, W. A.; Zhang, L.; Hoffman, B. M.; Peters, J. C. Characterization of an Fe≡N−NH_2 Intermediate Relevant to Catalytic N_2 Reduction to NH_3. *J. Am. Chem. Soc.* **2015**, *137* (24), 7803−7809.
(41) Saouma, C. T.; Kinney, R. A.; Hoffman, B. M.; Peters, J. C. Transformation of an $[Fe(\eta^2\text{-}N_2H_3)]^{+2}$ Species to π-Delocalized $[Fe_2(\mu\text{-}N_2H_2)]^{2++/++}$ Complexes. *Angew. Chem., Int. Ed.* **2011**, *50* (15), 3446−3449.
(42) Horitani, M.; Grubel, K.; McWilliams, S. F.; Stubbert, B. D.; Mercado, B. Q.; Yu, Y.; Gurubasavaraj, P. M.; Lees, N. S.; Holland, P. L.; Hoffman, B. M. ENDOR characterization of an iron-alkene

https://dx.doi.org/10.1021/jacs.0c05920
J. Am. Chem. Soc. 2020, 142, 18795−18813

complex provides insight into a corresponding organometallic intermediate of nitrogenase. *Chem. Sci.* **2017**, *8* (9), 5941−5948.
(43) Chiang, K. P.; Scarborough, C. C.; Horitani, M.; Lees, N. S.; Ding, K.; Dugan, T. R.; Brennessel, W. W.; Bill, E.; Hoffman, B. M.; Holland, P. L. Characterization of the Fe-H Bond in a Three-Coordinate Terminal Hydride Complex of Iron(I). *Angew. Chem., Int. Ed.* **2012**, *51* (15), 3658−3662.
(44) Citek, C.; Oyala, P. H.; Peters, J. C. Mononuclear Fe(I) and Fe(II) Acetylene Adducts and Their Reductive Protonation to Terminal Fe(IV) and Fe(V) Carbynes. *J. Am. Chem. Soc.* **2019**, *141* (38), 15211−15221.
(45) Gu, N. X.; Oyala, P. H.; Peters, J. C. An $S = 1/2$ Iron Complex Featuring N_2, Thiolate, and Hydride Ligands: Reductive Elimination of H_2 and Relevant Thermochemical Fe−H Parameters. *J. Am. Chem. Soc.* **2018**, *140* (20), 6374−6382.
(46) Hickey, A. K.; Greer, S. M.; Valdez-Moreira, J. A.; Lutz, S. A.; Pink, M.; DeGayner, J. A.; Harris, T. D.; Hill, S.; Telser, J.; Smith, J. M. A Dimeric Hydride-Bridged Complex with Geometrically Distinct Iron Centers Giving Rise to an $S = 3$ Ground State. *J. Am. Chem. Soc.* **2019**, *141*, 11970−11975.
(47) Yang, D.; Xu, S.; Zhang, Y.; Li, Y.; Li, Y.; Wang, B.; Qu, J. Reactivity toward Unsaturated Small Molecules of Thiolate-Bridged Diiron Hydride Complexes. *Inorg. Chem.* **2018**, *57* (24), 15198−15204.
(48) Yu, X.; Tung, C.-H.; Wang, W.; Huynh, M. T.; Gray, D. L.; Hammes-Schiffer, S.; Rauchfuss, T. B. Interplay between Terminal and Bridging Diiron Hydrides in Neutral and Oxidized States. *Organometallics* **2017**, *36* (11), 2245−2253.
(49) Yang, D.; Li, Y.; Wang, B.; Zhao, X.; Su, L.; Chen, S.; Tong, P.; Luo, Y.; Qu, J. Synthesis and Electrocatalytic Property of Diiron Hydride Complexes Derived from a Thiolate-Bridged Diiron Complex. *Inorg. Chem.* **2015**, *54* (21), 10243−10249.
(50) Lee, Y.; Anderton, K. J.; Sloane, F. T.; Ermert, D. M.; Abboud, K. A.; García-Serres, R.; Murray, L. J. Reactivity of Hydride Bridges in High-Spin [3M−3(μ-H)] Clusters (M = Fe^{II}, Co^{II}). *J. Am. Chem. Soc.* **2015**, *137* (33), 10610−10617.
(51) Rittle, J.; McCrory, C. C. L.; Peters, J. C. A 10^6-Fold Enhancement in N_2-Binding Affinity of an $Fe_2(\mu\text{-H})_2$ Core upon Reduction to a Mixed-Valence $Fe^{II}Fe^{I}$ State. *J. Am. Chem. Soc.* **2014**, *136* (39), 13853−13862.
(52) Wang, W.; Nilges, M. J.; Rauchfuss, T. B.; Stein, M. Isolation of a Mixed Valence Diiron Hydride: Evidence for a Spectator Hydride in Hydrogen Evolution Catalysis. *J. Am. Chem. Soc.* **2013**, *135* (9), 3633−3639.
(53) Jablonskytė, A.; Wright, J. A.; Fairhurst, S. A.; Peck, J. N. T.; Ibrahim, S. K.; Oganesyan, V. S.; Pickett, C. J. Paramagnetic Bridging Hydrides of Relevance to Catalytic Hydrogen Evolution at Metallosulfur Centers. *J. Am. Chem. Soc.* **2011**, *133* (46), 18606−18609.
(54) Yang, H.; Rittle, J.; Marts, A. R.; Peters, J. C.; Hoffman, B. M. ENDOR Characterization of $(N_2)Fe^{II}(\mu\text{-H})_2Fe^{I}(N_2)^-$: A Spectroscopic Model for N_2 Binding by the Di-μ-hydrido Nitrogenase Janus Intermediate. *Inorg. Chem.* **2018**, *57* (19), 12323−12330.
(55) Kinney, R. A.; Saouma, C. T.; Peters, J. C.; Hoffman, B. M. Modeling the Signatures of Hydrides in Metalloenzymes: ENDOR Analysis of a Di-iron Fe(μ-NH)(μ-H)Fe Core. *J. Am. Chem. Soc.* **2012**, *134* (30), 12637−12647.
(56) Robin, M. B.; Day, P., Mixed Valence Chemistry-A Survey and Classification. In *Advances in Inorganic Chemistry and Radiochemistry*; Emeleus, H. J., Sharpe, A. G., Eds.; Academic Press: 1968; Vol. *10*, pp 247−422.
(57) Holton, J.; Lappert, M. F.; Pearce, R.; Yarrow, P. I. W. Bridged hydrocarbyl or hydrocarbon binuclear transition metal complexes: classification, structures, and chemistry. *Chem. Rev.* **1983**, *83* (2), 135−201.
(58) Casey, C. P.; Fagan, P. J.; Miles, W. H. Synthesis and interconversions of dinuclear iron complexes with μ-methyl, μ-methylene, and μ-methylidyne ligands. *J. Am. Chem. Soc.* **1982**, *104* (4), 1134−1136.
(59) Marchetti, F. Constructing Organometallic Architectures from Aminoalkylidyne Diiron Complexes. *Eur. J. Inorg. Chem.* **2018**, *2018* (36), 3987−4003.
(60) Kuppuswamy, S.; Wofford, J. D.; Joseph, C.; Xie, Z.-L.; Ali, A. K.; Lynch, V. M.; Lindahl, P. A.; Rose, M. J. Structures, Interconversions, and Spectroscopy of Iron Carbonyl Clusters with an Interstitial Carbide: Localized Metal Center Reduction by Overall Cluster Oxidation. *Inorg. Chem.* **2017**, *56* (10), 5998−6012.
(61) Vollmer, G. Y.; Wallasch, M. W.; Saurenz, D.; Eger, T. R.; Bauer, H.; Wolmershäuser, G.; Prosenc, M. H.; Sitzmann, H. Benzylidyne Bridges from Diphenylacetylene and a Methylidyne Bridge from Methylmagnesium Chloride. *Organometallics* **2015**, *34* (3), 644−652.
(62) Wang, R.; Sun, J.; Chen, J.; Xu, Q.; Souma, Y. Unusual reactions of cationic bridging carbyne complexes of dimethylsilane-bridged bis(η^5-cyclopentadienyl)diiron tricarbonyl with carbonylmetal anions. *J. Organomet. Chem.* **2002**, *658* (1), 214−227.
(63) Mansuy, D.; Lecomte, J. P.; Chottard, J. C.; Bartoli, J. F. Formation of a complex with a carbide bridge between two iron atoms from the reaction of (tetraphenylporphyrin)iron(II) with carbon tetraiodide. *Inorg. Chem.* **1981**, *20* (9), 3119−3121.
(64) Tachikawa, M.; Muetterties, E. L. Metal clusters. 25. A uniquely bonded C-H group and reactivity of a low-coordinate carbidic carbon atom. *J. Am. Chem. Soc.* **1980**, *102* (13), 4541−4542.
(65) Churchill, M. R.; Wormald, J.; Knight, J.; Mays, M. J. Synthesis and crystallographic characterization of bis(tetramethylammonium) carbidohexadecacarbonylhexaferrate, a hexanuclear carbidocarbonyl derivative of iron. *J. Am. Chem. Soc.* **1971**, *93* (12), 3073−3074.
(66) Arnett, C. H.; Agapie, T. Activation of an Open Shell, Carbyne-Bridged Diiron Complex Toward Binding of Dinitrogen. *J. Am. Chem. Soc.* **2020**, *142*, 10059−10068.
(67) Yogendra, S.; Weyhermüller, T.; Hahn, A. W.; DeBeer, S. From Ylides to Doubly Yldiide-Bridged Iron(II) High Spin Dimers via Self-Protolysis. *Inorg. Chem.* **2019**, *58* (14), 9358−9367.
(68) Reesbeck, M. E.; Grubel, K.; Kim, D.; Brennessel, W. W.; Mercado, B. Q.; Holland, P. L. Diazoalkanes in Low-Coordinate Iron Chemistry: Bimetallic Diazoalkyl and Alkylidene Complexes of Iron(II). *Inorg. Chem.* **2017**, *56* (3), 1019−1022.
(69) Sun, C.-L.; Krause, H.; Fürstner, A. A Practical Procedure for Iron-Catalyzed Cross-Coupling Reactions of Sterically Hindered Aryl-Grignard Reagents with Primary Alkyl Halides. *Adv. Synth. Catal.* **2014**, *356* (6), 1281−1291.
(70) Ni, C.; Power, P. P. Methyl-Bridged Transition Metal Complexes (M = Cr-Fe) Supported by Bulky Terphenyl Ligands. *Organometallics* **2009**, *28* (22), 6541−6545.
(71) Klose, A.; Solari, E.; Floriani, C.; Chiesi-Villa, A.; Rizzoli, C.; Re, N. Magnetic Properties Diagnostic for the Existence of Iron(II)-Iron(II) Bonds in Dinuclear Complexes Which Derive from Stepwise Insertion Reactions on Unsupported Iron-Aryl Bonds. *J. Am. Chem. Soc.* **1994**, *116* (20), 9123−9135.
(72) Horitani, M.; Shisler, K.; Broderick, W. E.; Hutcheson, R. U.; Duschene, K. S.; Marts, A. R.; Hoffman, B. M.; Broderick, J. B. Radical SAM catalysis via an organometallic intermediate with an Fe−[5′-C]-deoxyadenosyl bond. *Science* **2016**, *352* (6287), 822−825.
(73) Wang, W.; Wang, K.; Li, J.; Nellutla, S.; Smirnova, T. I.; Oldfield, E. An ENDOR and HYSCORE Investigation of a Reaction Intermediate in IspG (GcpE) Catalysis. *J. Am. Chem. Soc.* **2011**, *133* (22), 8400−8403.
(74) Wang, W.; Li, J.; Wang, K.; Huang, C.; Zhang, Y.; Oldfield, E. Organometallic mechanism of action and inhibition of the 4Fe-4S isoprenoid biosynthesis protein GcpE (IspG). *Proc. Natl. Acad. Sci. U. S. A.* **2010**, *107* (25), 11189−11193.
(75) Ye, M.; Thompson, N. B.; Brown, A. C.; Suess, D. L. M. A Synthetic Model of Enzymatic [Fe4S4]−Alkyl Intermediates. *J. Am. Chem. Soc.* **2019**, *141* (34), 13330−13335.
(76) Li, J.; Wang, K.; Smirnova, T. I.; Khade, R. L.; Zhang, Y.; Oldfield, E. Isoprenoid Biosynthesis: Ferraoxetane or Allyl Anion Mechanism for IspH Catalysis? *Angew. Chem., Int. Ed.* **2013**, *52* (25), 6522−6525.

https://dx.doi.org/10.1021/jacs.0c05920
J. Am. Chem. Soc. 2020, 142, 18795−18813

(77) For the sake of comparison, the isoelectronic and structurally similar diiron μ-imide, μ-hydride complex ($[PhBP_3]Fe)_2(\mu$-NH)(μ-H)][Na(THF)$_5$] (ref 55, $PhBP_3^-$ = $PhB(CH_2PPh_2)_3^-$) displays electrochemical features at −2.58 V and −1.25 V. These are shifted by +200 mV and +400 mV, respectively, compared to corresponding redox events in (P_6ArC)$Fe_2(\mu$-H), consistent with the enhanced electron-releasing character of the carbyne ligand and the dialkylaryl-phosphine donors.
(78) Lee, Y.; Peters, J. C. Silylation of Iron-Bound Carbon Monoxide Affords a Terminal Fe Carbyne. *J. Am. Chem. Soc.* **2011**, *133* (12), 4438−4446.
(79) Bursten, B. E.; Cayton, R. H. Electronic structure of piano-stool dimers. 3. Relationships between the bonding and reactivity of the organically bridged iron dimers $[CpFe(CO)]_2(\mu$-CO)(μ-L) (L = CO, CH_2, C═CH_2, CH^+). *J. Am. Chem. Soc.* **1986**, *108* (26), 8241−8249.
(80) Dzik, W. I.; Zhang, X. P.; de Bruin, B. Redox Noninnocence of Carbene Ligands: Carbene Radicals in (Catalytic) C-C Bond Formation. *Inorg. Chem.* **2011**, *50* (20), 9896−9903.
(81) Chan, S.-C.; Gupta, P.; Engelmann, X.; Ang, Z. Z.; Ganguly, R.; Bill, E.; Ray, K.; Ye, S.; England, J. Observation of Carbodicarbene Ligand Redox Noninnocence in Highly Oxidized Iron Complexes. *Angew. Chem., Int. Ed.* **2018**, *57* (48), 15717−15722.
(82) Sharon, D. A.; Mallick, D.; Wang, B.; Shaik, S. Computation Sheds Insight into Iron Porphyrin Carbene' ' s' Electronic Structure, Formation, and N−H Insertion Reactivity. *J. Am. Chem. Soc.* **2016**, *138* (30), 9597−9610.
(83) Khade, R. L.; Fan, W.; Ling, Y.; Yang, L.; Oldfield, E.; Zhang, Y. Iron Porphyrin Carbenes as Catalytic Intermediates: Structures, Mössbauer and NMR Spectroscopic Properties, and Bonding. *Angew. Chem., Int. Ed.* **2014**, *53* (29), 7574−7578.
(84) Russell, S. K.; Hoyt, J. M.; Bart, S. C.; Milsmann, C.; Stieber, S. C. E.; Semproni, S. P.; DeBeer, S.; Chirik, P. J. Synthesis, electronic structure and reactivity of bis(imino)pyridine iron carbene complexes: evidence for a carbene radical. *Chem. Sci.* **2014**, *5* (3), 1168−1174.
(85) Jacobs, B. P.; Agarwal, R. G.; Wolczanski, P. T.; Cundari, T. R.; MacMillan, S. N. Fe(IV) alkylidenes are actually Fe(II), and a related octahedral Fe(II) ""alkylidene is a conjugated vinyl complex. *Polyhedron* **2016**, *116*, 47−56.
(86) Lindley, B. M.; Swidan, A. A.; Lobkovsky, E. B.; Wolczanski, P. T.; Adelhardt, M.; Sutter, J.; Meyer, K. Fe(IV) alkylidenes via protonation of Fe(II) vinyl chelates and a comparative Mössbauer spectroscopic study. *Chem. Sci.* **2015**, *6* (8), 4730−4736.
(87) Hartwig, J. F. *Organotransition Metal Chemistry: From Bonding to Catalysis*; University Science Books: Mill Valley, CA, 2010.
(88) Enemark, J. H.; Feltham, R. D. Principles of structure, bonding, and reactivity for metal nitrosyl complexes. *Coord. Chem. Rev.* **1974**, *13* (4), 339−406.
(89) Gibson, J. F.; Hall, D. O.; Thornley, J. H.; Whatley, F. R. The iron complex in spinach ferredoxin. *Proc. Natl. Acad. Sci. U. S. A.* **1966**, *56* (3), 987−990.
(90) Bencini, A.; Gatteschi, D. *Electron Paramagnetic Resonance of Exchange Coupled Systems*; Springer-Verlag Berlin Heidelberg: 1990.
(91) Bertrand, P.; Gayda, J.-P. A theoretical interpretation of the variations of some physical parameters within the [2Fe-2S] ferredoxin group. *Biochim. Biophys. Acta, Protein Struct.* **1979**, *579* (1), 107−121.
(92) McWilliams, S. F.; Bill, E.; Lukat-Rodgers, G.; Rodgers, K. R.; Mercado, B. Q.; Holland, P. L. Effects of N_2 Binding Mode on Iron-Based Functionalization of Dinitrogen to Form an Iron(III) Hydrazido Complex. *J. Am. Chem. Soc.* **2018**, *140* (27), 8586−8598.
(93) Safo, M. K.; Walker, F. A.; Raitsimring, A. M.; Walters, W. P.; Dolata, D. P.; Debrunner, P. G.; Scheidt, W. R. Axial Ligand Orientation in Iron(III) Porphyrinates: Effect of Axial π-Acceptors. Characterization of the Low-Spin Complex [Fe(TPP)(4-CNPy)$_2$]-ClO_4. *J. Am. Chem. Soc.* **1994**, *116* (17), 7760−7770.
(94) Brown, S. D.; Betley, T. A.; Peters, J. C. A Low-Spin d5 Iron Imide: Nitrene Capture by Low-Coordinate Iron(I) Provides the 4-Coordinate Fe(III) Complex $[PhB(CH_2PPh_2)_3]Fe$⋮N-p-tolyl. *J. Am. Chem. Soc.* **2003**, *125* (2), 322−323.
(95) Rieger, P. H. Electron paramagnetic resonance studies of low-spin d^5 transition metal complexes. *Coord. Chem. Rev.* **1994**, *135*−*136*, 203−286.
(96) McGarvey, B. R. Survey of ligand field parameters of strong field d^5 complexes obtained from the g matrix. *Coord. Chem. Rev.* **1998**, *170* (1), 75−92.
(97) Hyde, J. S.; Pasenkiewicz-Gierula, M.; Jesmanowicz, A.; Antholine, W. E. Pseudo field modulation in EPR spectroscopy. *Appl. Magn. Reson.* **1990**, *1* (3), 483.
(98) Although NMR demonstrates that the deuterium label was fully incorporated into methyl position of the ligand (Figure S24), ENDOR spectra of the cation and anion reveal that the μ-hydride site was only ∼50% enriched (Figures S66−68 for reference; also see Figure S32 and discussion therein). This discrepancy is attributed to slow isotopic scrambling during the synthesis of (P_6ArC)$Fe_2(\mu$-D), which may be facilitated by the elevated reaction temperatures. However, due to the different Larmor frequencies, the ^{2}H-labelled hydride can be selectively interrogated by HYSCORE such that the simulated parameters are not affected by the incomplete enrichment.
(99) The final ^{1,2}H hyperfine coupling tensor was obtained in an iterative process by simulating both the ^{2}H HYSCORE and ^{1}H ENDOR spectra.
(100) Epel, B.; Manikandan, P.; Kroneck, P. M. H.; Goldfarb, D. High-field ENDOR and the sign of the hyperfine coupling. *Appl. Magn. Reson.* **2001**, *21* (3), 287−297.
(101) Solomon, E. I. Inorganic Spectroscopy: High Resolution. *Comments Inorg. Chem.* **1984**, *3* (5), 288−300.
(102) McGarvey, B. R. The isotropic hyperfine interaction. *J. Phys. Chem.* **1967**, *71* (1), 51−66.
(103) Wertz, J. E.; Bolton, J. R. *Electron Spin Resonance: Elementary Theory and Practical Applications*; Chapman and Hall: New York, N.Y., 1986.
(104) Morton, J. R.; Preston, K. F. Atomic parameters for paramagnetic resonance data. *J. Magn. Reson.* **1978**, *30* (3), 577−582.
(105) Willems, J.-P.; Lee, H.-I.; Burdi, D.; Doan, P. E.; Stubbe, J.; Hoffman, B. M. Identification of the Protonated Oxygenic Ligands of Ribonucleotide Reductase Intermediate X by Q-Band ^{1,2}H CW and Pulsed ENDOR. *J. Am. Chem. Soc.* **1997**, *119* (41), 9816−9824.
(106) DeRose, V. J.; Liu, K. E.; Lippard, S. J.; Hoffman, B. M. Investigation of the Dinuclear Fe Center of Methane Monooxygenase by Advanced Paramagnetic Resonance Techniques: On the Geometry of DMSO Binding. *J. Am. Chem. Soc.* **1996**, *118* (1), 121−134.
(107) Hoeke, V.; Tociu, L.; Case, D. A.; Seefeldt, L. C.; Raugei, S.; Hoffman, B. M. Correction to ""High-Resolution ENDOR Spectroscopy Combined with Quantum Chemical Calculations Reveals the Structure of Nitrogenase Janus Intermediate E_4(4H). *J. Am. Chem. Soc.* **2019**, *141* (50), 19950−19950.
(108) Kinney, R. A.; Hetterscheid, D. G. H.; Hanna, B. S.; Schrock, R. R.; Hoffman, B. M. Formation of {[HIPTN$_3$N]Mo(III)H}$^-$ by Heterolytic Cleavage of H_2 as Established by EPR and ENDOR Spectroscopy. *Inorg. Chem.* **2010**, *49* (2), 704−713.
(109) Drover, M. W.; Schild, D. J.; Oyala, P. H.; Peters, J. C. Snapshots of a Migrating H-Atom: Characterization of a Reactive Iron(III) Indenide Hydride and its Nearly Isoenergetic Ring-Protonated Iron(I) Isomer. *Angew. Chem., Int. Ed.* **2019**, *58* (43), 15504−15511.
(110) Keizer, P. N.; Krusic, P. J.; Morton, J. R.; Preston, K. F. Thiolato- and selenato-bridged dinuclear iron carbonyl radicals. *J. Am. Chem. Soc.* **1991**, *113* (14), 5454−5456.
(111) Rao, G.; Altman, A. B.; Brown, A. C.; Tao, L.; Stich, T. A.; Arnold, J.; Britt, R. D. Metal Bonding with 3d and 6d Orbitals: An EPR and ENDOR Spectroscopic Investigation of Ti^{3+}−Al and Th^{3+}−Al Heterobimetallic Complexes. *Inorg. Chem.* **2019**, *58* (12), 7978−7988.
(112) The dipolar contribution to the coupling can be obtained from eqs 1−5 using the carbon gyromagnetic ratio. This affords an estimate of [−3.5, +1.1, +2.3] MHz, with the orientation of this tensor in the molecular frame undefined. It is not possible to explicitly determine the orientation of the ^{13}C hyperfine tensor in the molecular frame

https://dx.doi.org/10.1021/jacs.0c05920
J. Am. Chem. Soc. 2020, 142, 18795−18813

because of the convolution of both local and dipolar contributions. Given their nearly identical Fe−C bond lengths, the dipolar contribution to the ^{13}C hyperfine can be treated as a constant and neglected in the analysis. Although this may overestimate b, the redox-dependent trends should not be affected. In support of this assertion, the effect of redox on the DFT calculted Fe−C covalencies is in reasonable agreement with those inferred by EPR.

(113) Musgrave, K. B.; Angove, H. C.; Burgess, B. K.; Hedman, B.; Hodgson, K. O. All-Ferrous Titanium(III) Citrate Reduced Fe Protein of Nitrogenase: An XAS Study of Electronic and Metrical Structure. *J. Am. Chem. Soc.* **1998**, *120* (21), 5325−5326.

(114) Although edge energies are commonly regarded as an indicator of changes in relative oxidation state, the rising edge of some [Fe−S] clusters are invariant to redox chemistry. Detailed spectroscopic investigation of a series of [2Fe−2S] model complexes suggested that this behavior may arise as a consequence of valence localization (see ref 12). The distinct edge energies observed here are consistent with electronic delocalization. We note, however, that an increase in whiteline intensity (absorption past the rising edge) appears to be characteristic of iron-centered reduction in [Fe−S] clusters (again see ref 12). The opposite trend is observed here, with the most oxidized compound exhibiting the highest whiteline intensity (see Figure S51). As a result, it seems that this trend is system dependent and, thus, not fully generalizable.

(115) Baker, M. L.; Mara, M. W.; Yan, J. J.; Hodgson, K. O.; Hedman, B.; Solomon, E. I. K- and L-edge X-ray absorption spectroscopy (XAS) and resonant inelastic X-ray scattering (RIXS) determination of differential orbital covalency (DOC) of transition metal sites. *Coord. Chem. Rev.* **2017**, *345*, 182−208.

(116) Westre, T. E.; Kennepohl, P.; DeWitt, J. G.; Hedman, B.; Hodgson, K. O.; Solomon, E. I. A Multiplet Analysis of Fe K-Edge 1s → 3d Pre-Edge Features of Iron Complexes. *J. Am. Chem. Soc.* **1997**, *119* (27), 6297−6314.

(117) Chandrasekaran, P.; Stieber, S. C. E.; Collins, T. J.; Que, L., Jr.; Neese, F.; DeBeer, S. Prediction of high-valent iron K-edge absorption spectra by time-dependent Density Functional Theory. *Dalton Trans.* **2011**, *40* (42), 11070−11079.

(118) DeBeer George, S.; Petrenko, T.; Neese, F. Prediction of Iron K-Edge Absorption Spectra Using Time-Dependent Density Functional Theory. *J. Phys. Chem. A* **2008**, *112* (50), 12936−12943.

(119) Note that while TD-DFT performs well for metal localized transitions, charge transfer artifacts are common for systems with extended arylic π systems. For this reason, we focus on the true on the carbyne ligand, which can act as a true π acceptor.

(120) Rees, J. A.; Martin-Diaconescu, V.; Kovacs, J. A.; DeBeer, S. X-ray Absorption and Emission Study of Dioxygen Activation by a Small-Molecule Manganese Complex. *Inorg. Chem.* **2015**, *54* (13), 6410−6422.

(121) Roemelt, M.; Beckwith, M. A.; Duboc, C.; Collomb, M.-N.; Neese, F.; DeBeer, S. Manganese K-Edge X-Ray Absorption Spectroscopy as a Probe of the Metal−Ligand Interactions in Coordination Compounds. *Inorg. Chem.* **2012**, *51* (1), 680−687.

(122) Gütlich, P.; Bill, E.; Trautwein, A. X. *Mössbauer Spectroscopy and Transition Metal Chemistry: Fundamentals and Applications*; Springer: Berlin, 2011.

(123) Chalkley, M. J.; Peters, J. C. A Triad of Highly Reduced, Linear Iron Nitrosyl Complexes: $\{FeNO\}^{8-10}$. *Angew. Chem., Int. Ed.* **2016**, *55* (39), 11995−11998.

(124) Hay, P. J.; Thibeault, J. C.; Hoffmann, R. Orbital interactions in metal dimer complexes. *J. Am. Chem. Soc.* **1975**, *97* (17), 4884−4899.

(125) Brunold, T. C.; Gamelin, D. R.; Solomon, E. I. Excited-State Exchange Coupling in Bent Mn(III)-O-Mn(III) Complexes: Dominance of the π/σ Superexchange Pathway and Its Possible Contributions to the Reactivities of Binuclear Metalloproteins. *J. Am. Chem. Soc.* **2000**, *122* (35), 8511−8523.

(126) Gamelin, D. R.; Bominaar, E. L.; Kirk, M. L.; Wieghardt, K.; Solomon, E. I. Excited-State Contributions to Ground-State Properties of Mixed-Valence Dimers: Spectral and Electronic-Structural Studies of $[Fe_2(OH)_3(tmtacn)_2]^{2++}$ Related to the $[Fe_2S_2]^{+2}$ Active Sites of Plant-Type Ferredoxins. *J. Am. Chem. Soc.* **1996**, *118* (34), 8085−8097.

(127) Summerville, R. H.; Hoffmann, R. Tetrahedral and other M_2L_6 transition metal dimers. *J. Am. Chem. Soc.* **1976**, *98* (23), 7240−7254.

(128) Increasing the amount of exact exchange in the functional to 25% (TPSS0) affords an additional pair of magnetic orbitals (0.89). Inspection of the corresponding orbitals suggests that an additional resonance form, involving spin coupling of two $S = 1$ Fe(II) sites to a ligand-based radical, may also contribute to the ground state. The magnitude of the ^{13}C hyperfine indicates this contribution must be small.

(129) Blondin, G.; Girerd, J. J. Interplay of electron exchange and electron transfer in metal polynuclear complexes in proteins or chemical models. *Chem. Rev.* **1990**, *90* (8), 1359−1376.

(130) Orio, M.; Mouesca, J.-M. Variation of Average g Values and Effective Exchange Coupling Constants among [2Fe-2S] Clusters: A Density Functional Theory Study of the Impact of Localization (Trapping Forces) versus Delocalization (Double-Exchange) as Competing Factors. *Inorg. Chem.* **2008**, *47* (12), 5394−5416.

(131) Dey, A.; Glaser, T.; Moura, J. J. G.; Holm, R. H.; Hedman, B.; Hodgson, K. O.; Solomon, E. I. Ligand K-edge X-ray Absorption Spectroscopy and DFT Calculations on $[Fe_3S_4]^{0,++}$ Clusters: Delocalization, Redox, and Effect of the Protein Environment. *J. Am. Chem. Soc.* **2004**, *126* (51), 16868−16878.

(132) Glaser, T.; Rose, K.; Shadle, S. E.; Hedman, B.; Hodgson, K. O.; Solomon, E. I. S K-edge X-ray Absorption Studies of Tetranuclear Iron-Sulfur Clusters: μ-Sulfide Bonding and Its Contribution to Electron Delocalization. *J. Am. Chem. Soc.* **2001**, *123* (3), 442−454.

(133) Fu, W.; Drozdzewski, P. M.; Davies, M. D.; Sligar, S. G.; Johnson, M. K. Resonance Raman and magnetic circular dichroism studies of reduced [2Fe-2S] proteins. *J. Bio. Chem.* **1992**, *267* (22), 15502−15510.

(134) Han, S.; Czernuszewicz, R. S.; Kimura, T.; Adams, M. W. W.; Spiro, T. G. Fe_2S_2 protein resonance Raman spectra revisited: structural variations among adrenodoxin, ferredoxin, and red paramagnetic protein. *J. Am. Chem. Soc.* **1989**, *111* (10), 3505−3511.

(135) Brown, S. D.; Mehn, M. P.; Peters, J. C. Heterolytic H_2 Activation Mediated by Low-Coordinate L_3Fe-(μ-N)-FeL_3 Complexes to Generate Fe(μ-NH)(μ-H)Fe Species. *J. Am. Chem. Soc.* **2005**, *127* (38), 13146−13147.

(136) Noodleman, L.; Peng, C. Y.; Case, D. A.; Mouesca, J. M. Orbital interactions, electron delocalization and spin coupling in iron-sulfur clusters. *Coord. Chem. Rev.* **1995**, *144*, 199−244.

(137) Boča, R. Zero-field splitting in metal complexes. *Coord. Chem. Rev.* **2004**, *248* (9), 757−815.

(138) Scott, A. D.; Pelmenschikov, V.; Guo, Y.; Yan, L.; Wang, H.; George, S. J.; Dapper, C. H.; Newton, W. E.; Yoda, Y.; Tanaka, Y.; Cramer, S. P. Structural Characterization of CO-Inhibited Mo-Nitrogenase by Combined Application of Nuclear Resonance Vibrational Spectroscopy, Extended X-ray Absorption Fine Structure, and Density Functional Theory: New Insights into the Effects of CO Binding and the Role of the Interstitial Atom. *J. Am. Chem. Soc.* **2014**, *136* (45), 15942−15954.

(139) Pelmenschikov, V.; Case, D. A.; Noodleman, L. Ligand-Bound S = 1/2 FeMo-Cofactor of Nitrogenase: Hyperfine Interaction Analysis and Implication for the Central Ligand X Identity. *Inorg. Chem.* **2008**, *47* (14), 6162−6172.

(140) George, S. J.; Barney, B. M.; Mitra, D.; Igarashi, R. Y.; Guo, Y.; Dean, D. R.; Cramer, S. P.; Seefeldt, L. C. EXAFS and NRVS Reveal a Conformational Distortion of the FeMo-cofactor in the MoFe Nitrogenase Propargyl Alcohol Complex. *J. Inorg. Biochem.* **2012**, *112*, 85−92.

(141) Dance, I. Ramifications of C-centering rather than N-centering of the active site FeMo-co of the enzyme nitrogenase. *Dalton Trans.* **2012**, *41* (16), 4859−4865.

(142) Creutz, S. E.; Peters, J. C. Catalytic Reduction of N_2 to NH_3 by an Fe−N2 Complex Featuring a C-Atom Anchor. *J. Am. Chem. Soc.* **2014**, *136* (3), 1105−1115.

https://dx.doi.org/10.1021/jacs.0c05920
J. Am. Chem. Soc. 2020, 142, 18795−18813

(143) Rittle, J.; Peters, J. C. Fe−N_2/CO complexes that model a possible role for the interstitial C atom of FeMo-cofactor (FeMoco). *Proc. Natl. Acad. Sci. U. S. A.* **2013**, *110* (40), 15898−15903.
(144) Grunenberg, J. The Interstitial Carbon of the Nitrogenase FeMo Cofactor is Far Better Stabilized than Previously Assumed. *Angew. Chem., Int. Ed.* **2017**, *56* (25), 7288−7291.
(145) Rees, J. A.; Bjornsson, R.; Kowalska, J. K.; Lima, F. A.; Schlesier, J.; Sippel, D.; Weyhermuller, T.; Einsle, O.; Kovacs, J. A.; DeBeer, S. Comparative electronic structures of nitrogenase FeMoco and FeVco. *Dalton Trans.* **2017**, *46* (8), 2445−2455.
(146) Formanuik, A.; Ariciu, A.-M.; Ortu, F.; Beekmeyer, R.; Kerridge, A.; Tuna, F.; McInnes, E. J. L.; Mills, D. P. Actinide covalency measured by pulsed electron paramagnetic resonance spectroscopy. *Nat. Chem.* **2017**, *9* (6), 578−583.
(147) Potapov, A.; Lancaster, K. M.; Richards, J. H.; Gray, H. B.; Goldfarb, D. Spin Delocalization Over Type Zero Copper. *Inorg. Chem.* **2012**, *51* (7), 4066−4075.
(148) Bersohn, R.; Shulman, R. G. Measures of Covalency in Transition-Metal Chlorides. *J. Chem. Phys.* **1966**, *45* (6), 2298−2303.
(149) Lukoyanov, D.; Pelmenschikov, V.; Maeser, N.; Laryukhin, M.; Yang, T. C.; Noodleman, L.; Dean, D. R.; Case, D. A.; Seefeldt, L. C.; Hoffman, B. M. Testing if the Interstitial Atom, X, of the Nitrogenase Molybdenum-Iron Cofactor Is N or C: ENDOR, ESEEM, and DFT Studies of the S = 3/2 Resting State in Multiple Environments. *Inorg. Chem.* **2007**, *46* (26), 11437−11449.
(150) Dey, A.; Glaser, T.; Couture, M. M. J.; Eltis, L. D.; Holm, R. H.; Hedman, B.; Hodgson, K. O.; Solomon, E. I. Ligand K-Edge X-ray Absorption Spectroscopy of $[Fe_4S_4]$1+,2+,3+ Clusters: Changes in Bonding and Electronic Relaxation upon Redox. *J. Am. Chem. Soc.* **2004**, *126* (26), 8320−8328.

https://dx.doi.org/10.1021/jacs.0c05920
J. Am. Chem. Soc. 2020, 142, 18795−18813